
Wesleyan University

**Blue Skies Through a Blue Sky:
An Attempt To Detect
Rayleigh Scattering in the
Atmospheres of Extrasolar Planets
Using a Ground-Based Telescope**

by

Kristen Luchsinger

A thesis submitted to the
faculty of Wesleyan University
in partial fulfillment of the requirements for the
Degree of Master of Arts in Astronomy
with a Planetary Science Concentration

Middletown, Connecticut

April, 2017

Acknowledgements

I would like to thank the Astronomy department at Wesleyan University, which has been incredibly supportive during my time here. Both the faculty and the student community have been both welcoming and encouraging, and always pushed me to learn more than I thought possible.

I would especially like to thank Avi Stein and Hannah Fritze, who first made me feel welcome in the department, and Girish Duvurri and Rachel Aranow, who made the department a joyful place to be. They, along with Wilson Cauley, were always willing to talk through any issues I encountered with me, and I am sure I would not have produced nearly as polished a product without their help.

I would also like to thank the telescope operators, staff, and fellow observers from the time I spent at Kitt Peak National Observatory. Through their support and friendliness, they turned what could have been an overwhelming and frightening experience into a successful and enjoyable first ever solo observing run.

I would like to thank my advisor, Seth Redfield, for his constant support and encouragement. Despite leading three undergraduate and one graduate student through four theses on three different topics, Seth kept us all moving forward, usually even with a smile and constant, genuine enthusiasm for the science. During my time at Wesleyan, Seth was always aggressively supportive and welcoming, and I could not appreciate his mentorship more.

I would finally like to thank my mom, my sister, and my brother. Their love and support, even from over three thousand miles away, always keeps me grounded.

Contents

1	Introduction	1
1.1	Exoplanets Overview	2
1.2	Detection	2
1.2.1	Radial Velocity	3
1.2.2	Transits	5
1.3	Rayleigh Scattering	7
1.4	Telescopes	9
1.5	Planets	11
1.5.1	WASP 12b	11
1.5.2	HD 189733b	12
1.5.3	GJ3470b	12
1.6	Summary of Contents	13
2	Observations and Reduction	14
2.1	Instrumentation	14
2.2	Data Reduction	15
2.2.1	Biases, Flats, Darks	15
2.2.2	Spectroscopy	16
2.2.3	Red Light Loss	16
2.3	Observations	17
2.4	WASP 12	17

2.4.1	February 11th, 2016	18
2.4.2	February 12th, 2016	18
2.5	HD189733b	18
2.5.1	July 1st, 2016	19
2.6	GJ3470b	19
2.6.1	January 3rd, 2016	19
2.6.2	January 13th, 2016	20
2.7	Final Test	20
3	Diagnostics	24
3.1	Reference Stars	24
3.1.1	RMS By Eye	25
3.1.2	Individual Reference Stars	26
3.1.3	Brightness	27
3.1.4	Spectral Type	27
3.1.5	Proximity	32
3.1.6	Increasing Number of Reference Stars	33
3.1.7	Final Selections	35
3.2	Data Contamination	38
3.2.1	Binaries	38
3.2.2	Wind	38
3.2.3	Lost Data Points	39
3.2.4	Telluric Lines	39
4	Analysis - White Light	41
4.1	General Method	41
4.1.1	Reduction	41

4.1.2	Modeling	42
4.2	WASP 12	45
4.3	HD 189733	47
4.4	GJ 3470	49
5	Analysis - Spectra	51
5.1	Transit Detection	51
5.1.1	Wavelength Dependence	51
5.1.2	Rayleigh Scattering	51
5.2	Analysis of Transit Detections	52
5.2.1	WASP 12	52
5.3	Analysis of Transit Non-Detections	56
5.3.1	WASP 12	56
5.3.2	HD 189733	58
5.3.3	GJ 3470	58
6	Summary and Conclusions	61
6.1	Instrumentation	61
6.1.1	Transit Detection	61
6.1.2	Transmission Spectrum	62
6.1.3	Ground Based Telescopes	62
6.2	Future Work	63
6.2.1	Potential Improvements	63
6.2.2	Value of Future Attempts	64
6.3	Conclusions	65
	Bibliography	67

1 Introduction

Even though human beings are found exclusively on one planet, the planet Earth, we have always dreamed of exploring and living on other, alien planets. From colonies on Mars to invaders from distant reaches of the galaxy, our imaginations are captivated by the idea of life on other planets. As technology advanced, our interest in alien life has only increased as we have discovered new planets to dream about.

The first planet around a star like our own was discovered in 1995 (Mayor & Queloz 1995), and in the twenty years since, we have discovered another couple thousand extrasolar planets (also known as exoplanets). These exoplanets offer us immeasurable fodder for imagination. But as we discover more planets, we become curious as to the conditions on that planet. We want to know what we would experience if we ourselves were to stand on that planet. What would we feel under our feet? What would we see when we looked around? What air would we breathe?

Though we have the technology to detect these planets, we do not yet have the ability to answer all of our questions to the degree our curiosity demands. We can only begin to scratch the surface of what these new worlds are like. But our technology improves every day, and we are pushing the boundaries of what we can know further and further all the time. Questions about the conditions on exoplanets will soon be answerable.

1.1 Exoplanets Overview

The first exoplanet was detected around a pulsar (Wolszczan 1992), which is the massive, rapidly rotating remnant of a star which reached the end of its ability to burn fuel and became a supernova. These remnants are called neutron stars, since they are composed entirely of neutrons, and are second in density only to black holes. Pulsars are highly magnetized, and because of this, emit a tight beam of radio emission which can be seen whenever the star rotates so that its beam points directly at Earth. These stars rotate quickly, with periods as short as milliseconds. These short periods cause the stars to appear to pulse, periodically becoming much brighter for a brief moment.

The first exoplanet was detected by carefully timing the pulses of the pulsar, which would be altered by the gravitational perturbations of the orbit of a planet around the star. However, pulsar planets are not as interesting to us as humans, since they are not like our own planet and are not likely to be habitable. We want to discover planets around stars like our own, that is, stars which are about the same size and temperature as our Sun, which would allow us to put our own Solar System experiences in context.

1.2 Detection

So what is the technology which allows us to detect and study exoplanets? Astronomers use a handful of techniques, which all are better at detecting certain types of planets and which all tell us different information about the planets they detect. I will discuss the two detection methods which have had the most success thus far, namely, the radial velocity and transit methods of planet detection, which

have detected hundreds and thousands of exoplanets, respectively.

1.2.1 Radial Velocity

The first exoplanet detected around a main sequence star was detected by the radial velocity method (Mayor & Queloz 1995). The radial velocity method is similar to the method used to detect pulsar planets in that we look for the effects of gravitational perturbation on the star by a planet in orbit around its star. However, instead of timing pulses, with the radial velocity method, we are measuring shifts of the wavelengths of the spectral lines of stars. These shifts occur when the star is moving directly away from or directly towards us, and are also known as a Doppler shift. When the star is moving towards us, the wavelength shifts towards bluer wavelengths (blueshift), and it shifts towards redder wavelengths (redshift) when the star is moving away from us.

If a planet is in orbit around the star, its gravitational force will have an effect on the star. The star will move in a much smaller orbit around the center of the combined mass of the star and the planet. As long as the star's orbit is not inclined relative to our line of sight - that is, not face-on - the star will sometimes be moving away from us, and sometimes it will be moving towards us. We can observe this motion by tracking how its spectral lines shift back and forth as the star moves on its orbit, as seen in Figure 1.1.

The amplitude of the spectral line shift is determined by Equation 1.1:

$$K = \frac{28.4329 \text{ m s}^{-1}}{\sqrt{1 - e^2}} \frac{m_2 \sin i}{M_J} \left(\frac{m_1 + m_2}{M_{Sun}} \right)^{-2/3} \frac{P}{1 \text{ yr}}^{-1/3}, \quad (1.1)$$

where K is the semiamplitude, or the amplitude of the spectral shift in either direction (negative or positive) away from the zero point (the normal wavelength

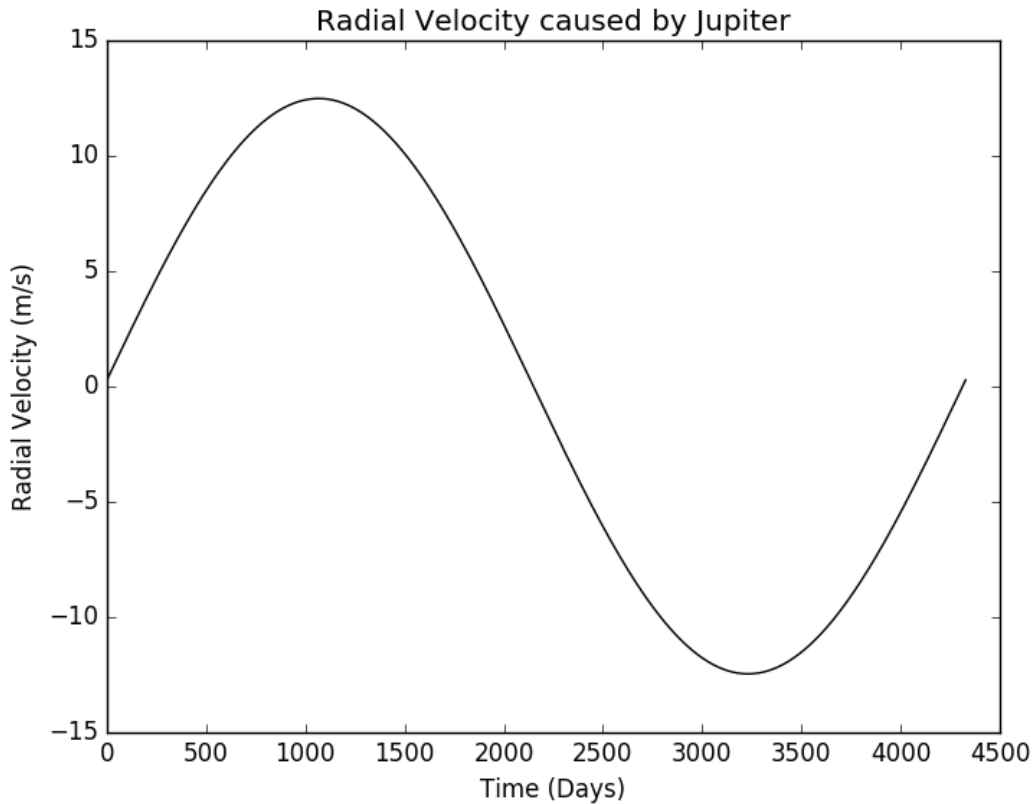


Figure 1.1: Radial velocity signature of Jupiter around the Sun. This figure shows the shift of one stellar spectral line. When the shift is negative, the light from the star is blueshifted, which means that the star is moving towards us and the planet is moving away from us in their orbits. When the shift is positive, the opposite is true - the light from the star is redshifted, so the star is moving away from us and the planet is moving towards us on their orbits. We can measure the period of the planet's orbit by measuring how long it takes for the shift to return to its starting point - 4328.9 days, in the case of Jupiter - and estimate the eccentricity of the orbit by measuring how close the curve of the changing shift is to a sine curve - 0.048, in the case of Jupiter. The closer the curve is to a sine wave, the less eccentric the orbit is, and vice versa. We can also measure the ratio of the mass of the planet to the mass of the star by measuring the amplitude of the curve, and then using Equation 1.1 to find the ratio. If we know the mass of the star, which we can determine using other observations, we can then find the mass of the planet.

of the spectral line), e is the eccentricity of the planet's orbit, i is the inclination of the planet's orbit to our line of sight (where 90 degrees is edge on, and zero degrees is face on), m_2 is the mass of the planet, M_J is the mass of Jupiter, m_1 is the mass of the planet's host star, M_{Sun} is the mass of our Sun, and P is the period of the planet's orbit.

Using this equation, if we know the mass of the star - which we can find based on its spectral type - and the period of the orbit - which we can find based on the period of the oscillation of the spectral line - we can determine the mass of the planet multiplied by the sine of its inclination. Because the mass and the inclination are tied together, we cannot find the exact mass, but we can constrain it based on this measurement.

The radial velocity method favors massive planets in short periods - that is, close to their stars - around low mass stars. Because of this, it is not an ideal method for finding Earth-mass planets in orbits with periods close to that of the Earth's, which are the types of planets we as humans are most interested in studying. However, the radial velocity method plays a crucial role in shaping our understanding of the types and numbers of planets that form in our universe, and allowed our study of exoplanets to quickly advance.

1.2.2 Transits

The most successful method of studying exoplanets thus far has been the transit method, by which we have detected multiple thousands of exoplanets. This method observes transit events where a planet will pass between our line of sight and its host star, causing a temporary dip in the flux, or brightness, we observe from the star, as seen in Figure 1.2. The transit depth, or the fraction of

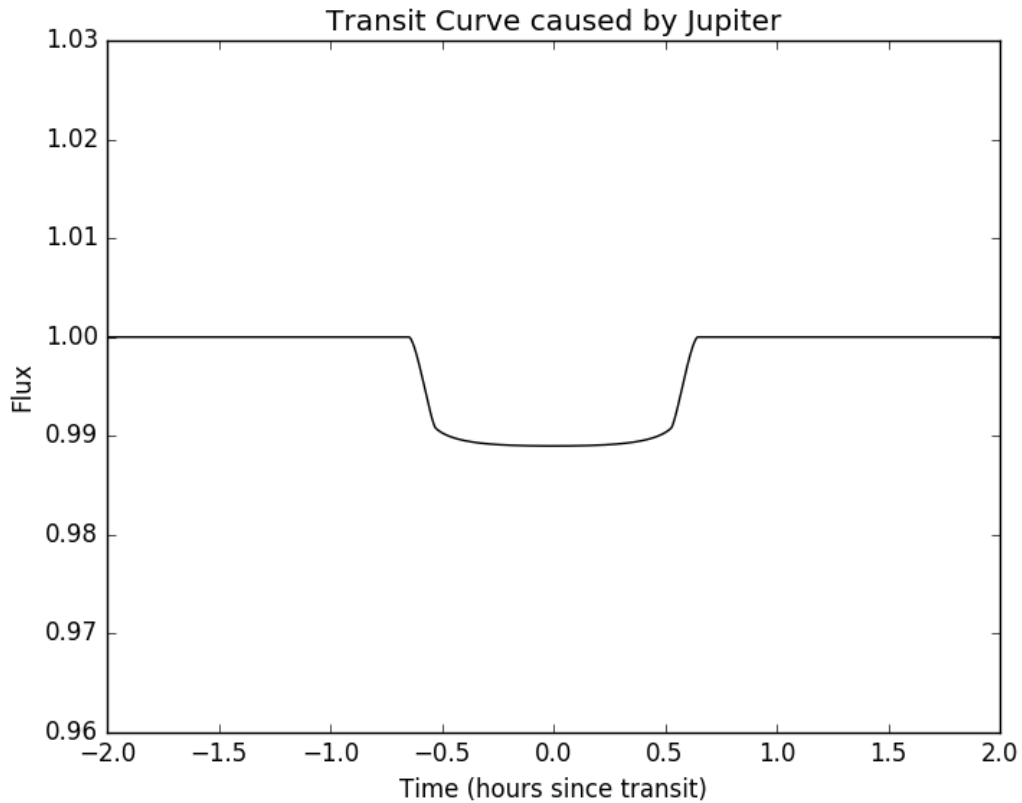


Figure 1.2: Transit signature of Jupiter around the Sun. This figure shows the drop in flux from the star as the planet moves across the face of the star. The depth of the drop in flux depends on the ratio of the radius of the planet to the radius of the star, since this ratio determines how much of the face of the star is blocked by the face of the planet during the transit. This transit curve was calculated using the Kreidberg (2015) `batman` python module.

light blocked during the transit event, is determined by the ratio of the area of the planet with the ratio of the area of the star which it is partially eclipsing, as seen in Equation 1.2:

$$\delta = \sqrt{\frac{R_p}{R_s}}. \quad (1.2)$$

The transit method, therefore, allows us to measure the radius of the planet if we know the radius of the star.

1.3 Rayleigh Scattering

I will be studying the atmospheres of three exoplanets, looking specifically for Rayleigh scattering. Rayleigh scattering, a familiar phenomenon on Earth, is caused by small particles in the atmosphere of a planet which scatter any light whose wavelength is larger than the particles themselves. In the atmosphere of the Earth, these small particles preferentially scatter bluer light, or light with a shorter wavelength, as compared to red light, as seen in Figure 1.3. The blue light which has been scattered will eventually hit the surface of the planet, but not from the direction of the Sun, since it has been scattered around the atmosphere before making its way to the surface of the planet.

This Rayleigh scattering effect causes the sky to appear to be blue, since the blue light from the Sun appears to us on the surface to come from the sky in general and not from the direction of the Sun. Rayleigh scattering is also the reason that although the Sun's emission peaks in green light, when we look from the surface of the Earth, the Sun appears to be yellow. When the light passes through the atmosphere, the yellow and red light is not scattered as much as the bluer light, so those wavelengths dominate the light which appears to us to have

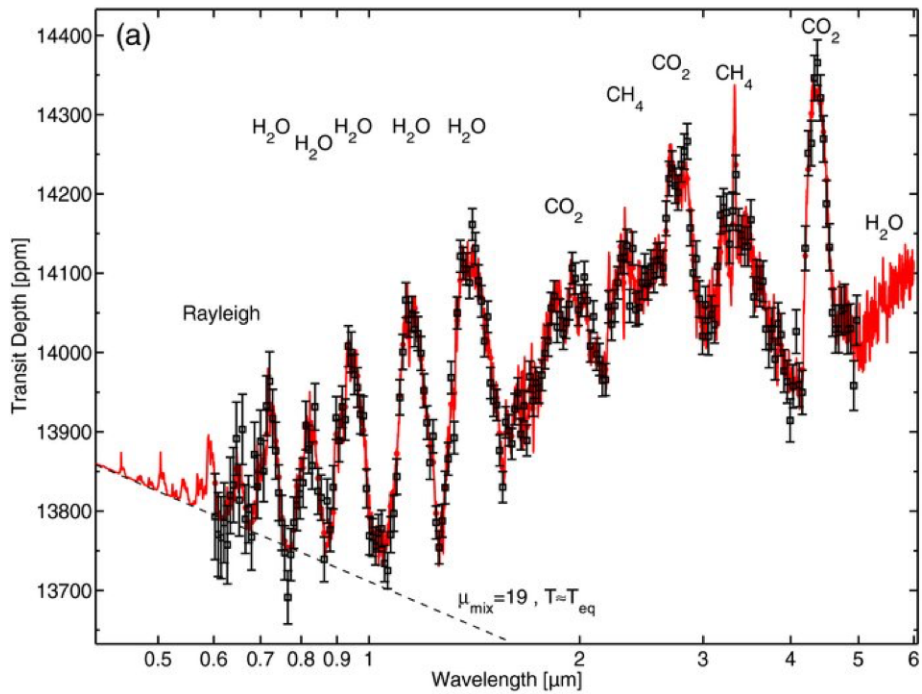


Figure 1.3: A modeled transmission spectrum of the exoplanet GJ 1214b. The dashed line in the lower left portion of the figure represents the Rayleigh scattering signature in the transmission spectrum. Although, the x-axis is in units of μm , which is equal to 10000 \AA , I will use \AA ngstroms in the rest of this paper. The larger features represent molecular signatures in the atmosphere. Figure originally from Benneke & Seager (2012).

come from the direction of the Sun.

We can use the transit method to detect Rayleigh scattering in exoplanet atmospheres, as well. Absorption or scattering causes the light which would otherwise pass through the atmosphere and reach our telescope to be blocked, and therefore, causes more light in total to be blocked by the planet. We would then measure a larger total radius of the planet. In order to study the atmospheres of exoplanets, then, we measure the radius of the exoplanet at various wavelengths. If a molecule which absorbs at a given wavelength λ is present in the atmosphere of the planet, the radius will appear to be larger at that wavelength than it would at a wavelength which no molecules existing in the atmosphere absorbed.

If an exoplanet has a Rayleigh scattering signature similar to that of the Earth's, then much more of the redder light which enters the atmosphere of the exoplanet should pass through the atmosphere to the telescope than the bluer light, which will be scattered into the atmosphere and will not pass through to the telescope. In order to detect Rayleigh scattering, we want to measure the radius of the planet at as many optical wavelengths as possible, so as to measure the slope caused by the Rayleigh scattering in the atmosphere of the exoplanet.

1.4 Telescopes

Exoplanet atmospheres are difficult to detect and measure, in part because the signals we need to measure are very small. The difference between the transit depth (the amount of flux from the star blocked by the exoplanet) and the changes in transit depth caused by the atmosphere of the planet is roughly 10^{-5} of the total flux received from the star. A typical transit depth is roughly 1% of the total flux, so our measurement of the transit depth needs to be very precise in

order to accurately identify a Rayleigh scattering slope.

The telescopes best suited to taking exoplanet atmosphere observations are the large, space-based telescopes such as the *Hubble Space Telescope*, the *Spitzer Space Telescope*, the *Kepler Space Telescope*, and the upcoming *James Webb Space Telescope*, since they do not need to worry about the effects of the atmosphere of the Earth on the data. These effects can wash out the very small atmospheric signals from the exoplanet. However, the space-based telescopes are also much more expensive and, because they are not affected by the Earth's atmosphere, are in much higher demand. When astronomers do get time on these space telescopes, it is important to use them to observe exoplanets which have the potential to be interesting science targets.

In order to identify these potentially interesting targets, astronomers have successfully used ground-based telescopes such as the 4.2 meter William Herschel Telescope, the Baade Telescope at Las Campanas Observatory, and the ESO La Silla 3.6 meter telescope (Kirk et al. 2016a; Jordán et al. 2013; Di Gloria et al. 2015) to detect Rayleigh scattering slopes in exoplanet atmospheres. These ground-based detections can inform the future use of space telescopes to investigate further and search for less prominent atmospheric features such as molecular or atomic absorption.

I used the Hydra spectrometer on the 3.5 meter WIYN telescope at Kitt Peak National Observatory. This instrument has not been used to study exoplanet atmospheres in the past, but could potentially be adapted to this use. I took observations of exoplanets with previous Rayleigh scattering detections so that I could try to replicate the previous detections using the WIYN telescope.

1.5 Planets

The three exoplanets I observed were WASP 12b, HD 189733b, and GJ 3470b. All three exoplanets' atmospheres have been studied extensively in the past, and all three of them have had successful detections of Rayleigh scattering signatures (Dragomir et al. 2015; Awiphan et al. 2016; Ehrenreich et al. 2014; Nascimbeni et al. 2013; Stevenson et al. 2014a,b; Copperwheat et al. 2013; Sing et al. 2013; Pont et al. 2013; Angerhausen et al. 2015; McCullough et al. 2014). I hope to determine, by studying these well characterized planets, whether the Kitt Peak WIYN telescope and the Hydra multi-object spectrometer can be used to study exoplanet atmospheres. I have included tables of the stellar and planetary properties of these systems in Tables 1.1 and 1.2.

1.5.1 WASP 12b

WASP 12b is a “hot Jupiter” - a large, Jupiter-like gaseous planet orbiting extremely close to its star at 0.02 AU (Chan et al. 2011), which is much closer than Mercury orbits our own Sun, at 0.387 AU. WASP 12b is one of the closest known planets to its star, which means that its extremely hot atmosphere should display many interesting absorption and scattering features. Its transit depth of 0.012 (Stevenson et al. 2014b) is significant enough to allow us to detect it with relative ease. The star around which the planet orbits, WASP 12, has a spectral type, mass, and radius which are all similar to that of our Sun, which makes WASP 12 an interesting target for continued study.

1.5.2 HD 189733b

HD 189733b is also a hot Jupiter, but orbits at a slightly further distance from its star than WASP 12b at 0.031 AU. HD 189733b is one of the closest known exoplanets to Earth at only 19.3 parsecs away, which means that even though its star has a spectral type of K0 and a mass of only 0.8 times the mass of the Sun, it is a bright star with deep transits. The proximity of HD 189733 to Earth is important, since it allows us to study this planet around a very small star, and small stars are preferable for studying transits, since the difference between their radii and the radii of their planets are minimized, which, from Equation 1.2, gives us a larger transit depth of 0.024 (Torres et al. 2008).

1.5.3 GJ3470b

The third planet, GJ 3470b, is not a hot Jupiter, but rather a “warm Neptune” - an icy planet about fourteen times the mass of the Earth orbiting extremely close to its star. GJ 3470b is one of the smallest planets ever to have a confirmed Rayleigh scattering detection (Dragomir et al. 2015), which makes its inclusion in this study an exciting opportunity to try to push the boundaries of our ability to detect atmospheres using a ground-based telescope. Its star, GJ 3470, is only 10 parsecs further away from us than HD 189733, at 29.3 parsecs away, and is has a spectral type of M2V and a mass and radius which are both about half that of the Sun’s. Although the star is close and has a small radius, GJ 3470b also has a smaller radius than WASP 12b or HD 189733b, which means that the transit depth produced by GJ 3470b is extremely small, at 0.0057 (Nascimbeni et al. 2013). Its atmosphere will be the most difficult of the three to study.

Table 1.1: Stellar Properties

<i>Name</i>	<i>Spectral Class</i>	<i>V Magnitude</i>	<i>Mass</i> (M_{\odot})	<i>Distance</i> (<i>pc</i>)
HD 189733	K0V	7.67	0.8	19.3
WASP 12	G0V	11.69	1.35	427.0
GJ 3470	M2V	12.27	0.54	29.28

Table 1.2: Planetary Properties

<i>Name</i>	<i>Mass</i> (M_J)	<i>Radius</i> (R_J)	<i>Semimajor</i> <i>Axis</i> (<i>AU</i>)	<i>Period</i> (<i>days</i>)
HD 189733b	1.13	1.14	0.03	2.22
WASP 12b	1.4	1.7	0.02	1.09
GJ 3470b	0.04	0.4	0.04	3.34

1.6 Summary of Contents

I will discuss our observations in Chapter 2, including the instruments used and our data reduction processes, and our methods for diagnostics and elimination of systemic errors in Chapter 3. In Chapters 4, 5, and 6, I will discuss the analysis of the observations for the three planets and the results produced by that analysis. Finally, I will present our overall results and findings, particularly as regards the future use of the Kitt Peak WIYN telescope and the Hydra bench spectrometer for Rayleigh scattering and other exoplanet atmosphere studies.

2 Observations and Reduction

2.1 Instrumentation

I used the Kitt Peak 3.5 meter WIYN telescope and the Hydra multiobject bench spectrometer for my observations (Barden et al. 2009). The Hydra spectrometer uses optical fibers placed at the positions of the objects to be observed and then transmits to the bench spectrograph, which uses a 2600×4000 CCD (charge coupled device) chip with $12\mu\text{m}$ pixels.

CCD cameras measure the number of accumulated photons per unit time per pixel. Each pixel measures how much light is coming from every star by measuring how many photons land on the pixel looking at that star every second. When a photon first hits the telescope, it travels down a fiber to the CCD chip, where it interacts with the silicon chip and provokes an electron in the silicon to disengage from its atom. All of the freed electrons are then measured, allowing me to measure the number of photons received by the pixels relative to one another.

Each column of pixels measures the full spectrum from one of the Hydra spectrometer fibers, so that the final image shows the flux from each fiber in parallel vertical lines along the chip, with the vertical axis corresponding to the wavelength. The horizontal location of a vertical line of flux on the chip is then matched back up with the fiber and its target during the data reduction.

2.2 Data Reduction

2.2.1 Biases, Flats, Darks

For each night of data, I took bias, flat, and dark images in order to properly reduce the data.

Bias images are images taken in the dark with zero seconds of exposure time. These images measure only the noise inherent to the sensors themselves, separate from any photons received by the sensors. Dark images are also images taken in the dark, but with an exposure time, to measure the ‘dark current’ present in the electronics of the sensors. The Bench Spectrometer has non-insignificant levels of dark current, which can become particularly problematic during long exposures. However, since all of my exposure times are 60 seconds or less, this will not be a major problem in my data reduction.

Flat images, unlike bias or dark images, are taken when an equal amount of white light shines through each fiber. This creates a flat field, which describes the differing reactions of each pixel. These reactions must be corrected for when reducing data. I also take images with light from a CuAr (Copper-Argon) calibration lamp shining on each pixel, and measure the response of each pixel to the same stimula in order to develop a wavelength solution for each fiber.

All three procedures - biases, darks, and flats - enable the measurement of the variations in the response of each pixel in the sensor to stimuli, whether the stimulus is the light received, the current present in the electronics controlling the sensor, or the noise present in the sensor itself. In order to properly reduce my images, I divide the flats and subtract the biases and darks from the observed data, removing the flat, bias, and dark signals from my final results.

2.2.2 Spectroscopy

The pixels on the chip each correspond to the flux of one star in one wavelength. The pixels with the same horizontal coordinate correspond to the same star, and taken together, build up the complete spectrum of that star between about 4000 Å and 9500 Å. The exact wavelength range will vary for each observation, and even between stars in one single observation. I can either sum up the flux received from the star in all of the pixels corresponding to that star - and therefore, all of the flux received from the star in all wavelengths, which is also known as the white light received from the star - or I can translate the pixels into wavelengths using their position on the chip to map out the spectrum of the star.

I use the CuAr calibration lamp images to determine a wavelength solution for each fiber. Since I know what emission lines are being detected by the fibers, I can match the observed emission lines with the wavelengths at which I know they have been emitted. Each fiber will have its own, unique wavelength solution, since the light will shine slightly differently on each fiber.

2.2.3 Red Light Loss

We used the blue fiber on the Hydra spectrometer, which introduces significant scatter in the redder light in our data. Transmission of light drops off non-uniformly when the silicon CCD chip becomes transparent to light at or above wavelengths of 8500 Å, which introduces uncertainty into the data (Barden et al. 2009).

2.3 Observations

The observations were taken both remotely and on site by myself, Dr. Seth Redfield, and Dr. Wilson Cauley. I was able to travel to Kitt Peak National Observatory to be on site for the July 1st observation of HD 189733, and was the sole observer on location during that observation. I was also the primary remote observer for the July 21st observation for HD 189733, though due to poor weather conditions, the telescope was unable to open. I have summarized the technical details of each observation, such as the date, observer, observing location, exposure time, and signal to noise (measured per pixel, per exposure) in Table 2.1, and I will go into more detail on each of the observations in sections 2.4, 2.5, and 2.6.

Table 2.1: Observations

<i>Target</i>	<i>Date (2016)</i>	<i>Observer</i>	<i>Location</i>	<i>Exposure Time</i>	<i>Signal to Noise</i>
GJ 3470	Jan. 3rd	S. Redfield	Remote	60 seconds	4
GJ 3470	Jan. 13th	S. Redfield	Remote	30 seconds	21
WASP 12	Feb. 11th	S. Redfield	Remote	45 seconds	168
WASP 12	Feb. 12th	W. Cauley	Remote	60 seconds	131
HD 189733	July 1st	K. Luchsinger	On Site	60 seconds	281
HD 189733	July 21st	K. Luchsinger	Remote

2.4 WASP 12

I worked with two observations of WASP 12, both of which captured the full transit of the planet WASP 12b. These two transits were taken remotely on February 11th and 12th by Dr. Seth Redfield and Dr. Wilson Cauley, respectively.

2.4.1 February 11th, 2016

The observation on February 11th, 2016 obtained data covering most of the transit, with the exception of 15 minutes' worth of data when the system passed through the "cone of avoidance" - a section of sky surrounding the zenith which the telescope could not slew through. The missing data points lie in the bottom of the transit, and do not obscure either ingress or egress. The weather was clear, and humidity was low throughout the night.

2.4.2 February 12th, 2016

The observations on the 12th of February were somewhat affected by clouds, which varied in thickness throughout the night, requiring the observer to change exposure times to keep up with the changing levels of flux received from the targets. The data were significantly affected by this bad weather, and scatter is present throughout the dataset.

2.5 HD189733b

HD 189733 is a nearby, and therefore bright, star, which means that observations of this star require shorter exposures in order to avoid saturation of the chip. I used an exposure time of 60 seconds for my observations of HD 189733. However, both transits of HD 189733b were scheduled in July. This posed a problem, since the weather in Arizona in July is dominated by the monsoon season. Although I had two nights of data, I was only able to utilize the first night, since the telescope was unable to open due to the weather conditions on July 21st. HD 189733b is, therefore, the only planet for which I was only able to observe one

night of data.

2.5.1 July 1st, 2016

I observed HD 189733 on site on July 1st. Despite observing during monsoon season, the weather on July 1st, 2016 was clear for most of the night. I was unable to open the dome initially due to thick clouds, but these lasted for less than an hour, and thick clouds did not reoccur during the rest of the night. Humidity was high, between 70 and 80 percent, the wind moderate and consistent, and we saw only the occasional puffy cloud.

Though the start of the observation was delayed, I was able to capture the full transit, three hours of post transit data, and about half an hour of pre-transit data.

2.6 GJ3470b

GJ 3470 is the dimmest and the reddest of the three stars, with a spectral type of M2V and an apparent V magnitude of 12.3 (Biddle et al. 2014). Both nights of observations were taken remotely by Dr. Seth Redfield.

2.6.1 January 3rd, 2016

The observations of GJ 3470 on January 3rd were sufficiently plagued with weather issues as to prohibit us from detecting the transit. Technical issues prevented the telescope from beginning its observations until about an hour before the transit began, and strong winds forced the telescope to shut down only two and a half hours after the start of the transit. The wind had caused the guide stars to disappear from view occasionally prior to this point, indicating that the

data were affected by the wind. Additionally, while the night began with only light cloud cover, the clouds thickened and became too thick to observe through at about the same time the wind forced the observers to shut down the telescope.

2.6.2 January 13th, 2016

The January 13th observation of GJ 3470 enjoyed much clearer weather than the January 3rd observations had, with only light wind and scattered clouds. Seeing conditions were about as good as could be expected, with an estimated seeing of about 1.1 arcseconds after midnight.

2.7 Final Test

Once the data had been reduced, I plotted the spectra of the target stars to check that the data reduction produced reasonable spectra for each star. I have included the spectra of the three target stars in Figures 2.1, 2.2, and 2.3. For the target stars with multiple observations, I selected the observation with the best weather conditions.

The spectra of WASP 12 and HD 189733, which were observed with signal to noise ratios of 281 and 168, respectively, are shown in Figures 2.1 and 2.2. The most dominant features in these two spectra are the telluric lines at 6900, 7250, and 7660 Å. The other features seen in the spectra are stellar lines associated with G0V and K0V stars, respectively, such as the H_β line at 4861 Å, which is present in the spectrum of WASP 12 and not in the spectrum of HD 189733. The peak wavelength of WASP 12 occurs around 6000 Å, compared to the redder HD 189733, which peaks around 6800 Å. These spectra are consistent with the spectra of G0V and K0V stars, respectively, and assure me that my data reduction process

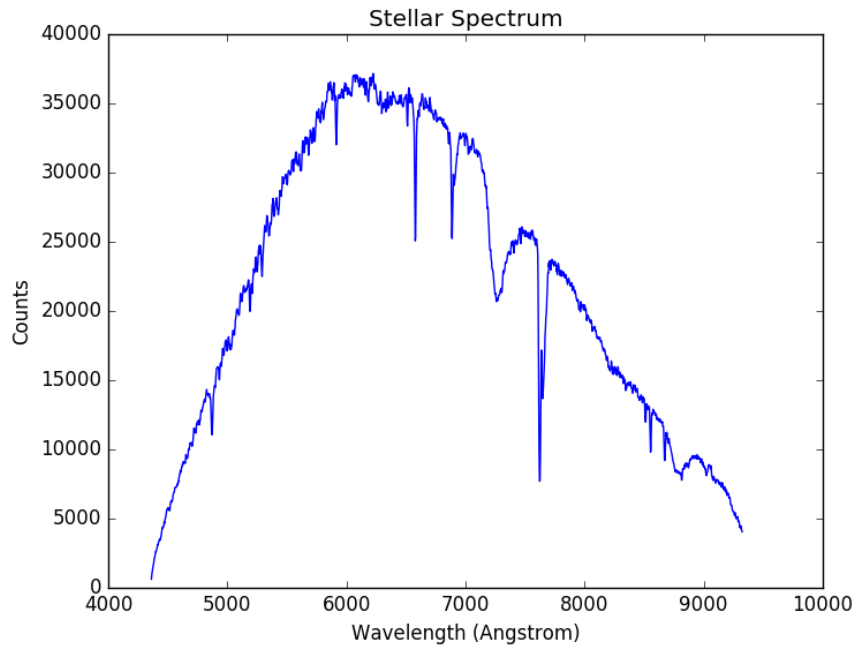


Figure 2.1: Spectrum of WASP 12 taken on February 11th, 2016.

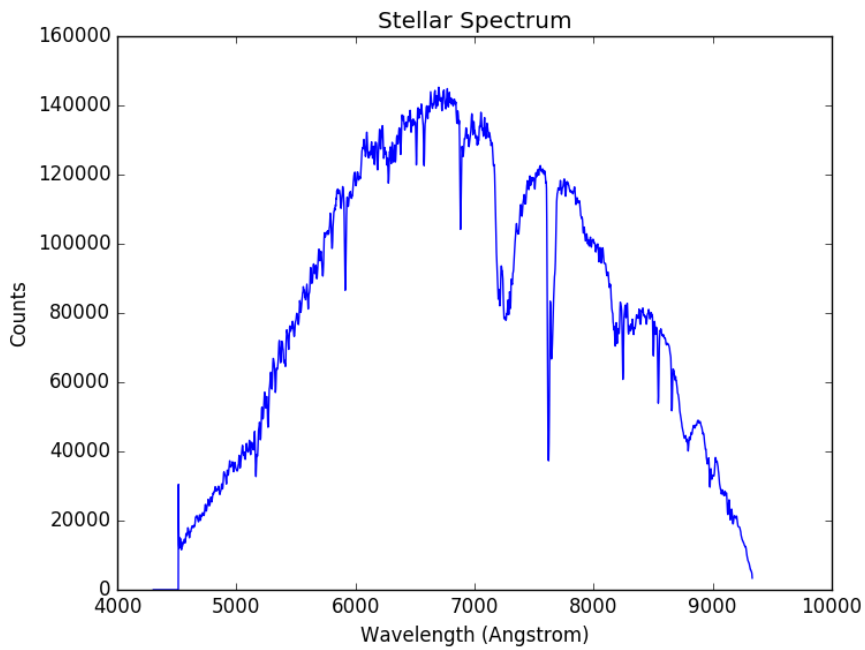


Figure 2.2: Spectrum of HD 189733 taken on July 1st, 2016.

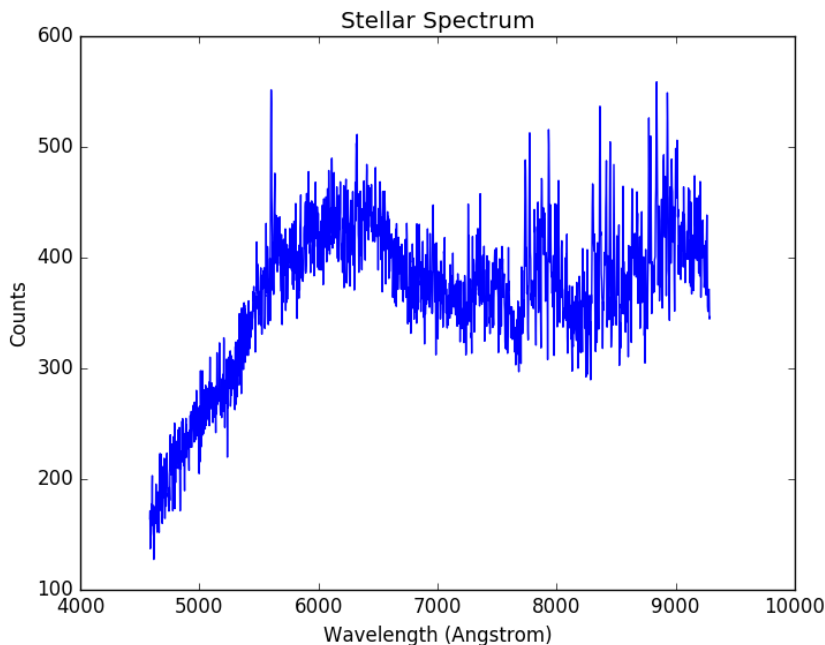


Figure 2.3: Spectrum of GJ 3470 taken on January 13th, 2016.

produced reasonable data.

The signal to noise ratios additionally indicate that these observations should, barring instrumental issues, be sufficiently resolved to detect a transit in these observations. There is more scatter in the spectrum of HD 189733 than in the spectrum of WASP 12, despite HD 189733 receiving a higher number of counts, which may lead to additional scatter in the light curves later on.

The spectrum of GJ 3470, plotted in Figure 2.3, is worrying, since the counts are low enough to introduce significant noise into the spectrum and cause it to deviate from the standard blaze function shape seen in the spectra of WASP 12 and HD 189733. However, the spectra of reference stars observed at the same time as GJ 3470 did receive the appropriate amount of flux, which means that a longer exposure time would have resulted in overexposed reference stars, which can bleed into neighboring fibers and ruin the data. Because the exposure time was limited

by brighter reference stars, GJ 3470 only achieved signal to noise ratio of 21. This led to the noisy spectrum and will lead to a non-detection of the transit.

3 Diagnostics

3.1 Reference Stars

Once my data were reduced, I added together and then subtracted the flux of several reference stars from the flux of my target star in order to remove any variations in the flux over the course of the night due to changing sky conditions. Since sky conditions affect both the target and reference stars, subtracting the flux should remove these variations. I added together multiple reference stars in order to smooth over any individual variations in the reference stars, but it was still important to choose reference stars that removed the sky variations without otherwise altering the light curve of the target star. I have included the light curves of GJ 3470 and the summed fluxes of the reference star in Figure 3.1. The light curves both show the onset of bad weather partway through the night, but also demonstrate that the small-scale variations earlier in the night are consistent between the target and reference stars. The reference stars are used to remove these small-scale variations.

I had between 50 and 60 possible reference stars for each target star, and I explored several different ways of selecting which of these reference stars to use to create my transit curves. I tested various parameters, including magnitude, proximity, and spectral type, to see which produced transit curves with the lowest rms or root mean square, under the assumption that the lowest rms would indicate a transit curve lacking in noise contamination.

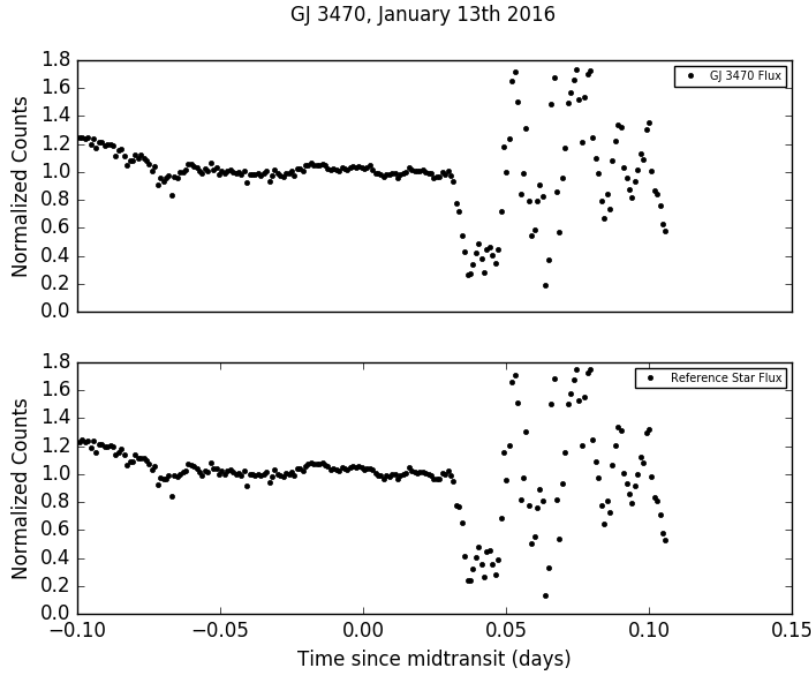


Figure 3.1: Light curves of GJ 3470 (top) and the summed reference star fluxes (bottom) from the January 13th observation.

For most methods, I was unable to select a set of reference stars for my GJ 3470 data which produced a transit light curve with a detectable transit due to the small signal to noise and weather interference for both nights. I have therefore not included my GJ 3470 results in the following discussions about reference star selection method. Since none of my reference star selection methods were able to eliminate enough noise to see a transit, including the GJ 3470 data would not provide insight into which reference star selection method produced the best transit curves.

3.1.1 RMS By Eye

The first method I used for each target was a simple minimization of root mean square, that is, rms, by eye, for the out of transit portion of the transit

light curve. The root mean square measures the scatter in this data, so since the best reference stars should minimize the scatter, a low rms should indicate a good selection of reference stars.

I began my minimization by eye by selecting one decent reference star, tried it in combination with all other possible reference stars, and kept any stars which lowered the rms. I then tested the first, randomly chosen star to see if removing it from the pool improved or worsened the rms, and if so, tried all others again, this time in combination with the remaining reference stars. At the end of this process, I had between three and five stars which, combined, produced the lowest rms.

This process, while relatively effective, was informal, and I therefore had no guarantee that the reference stars I chose were the best possible reference stars, and no way to choose reference stars without making a judgement about the transit curve produced. I therefore established two procedures to test reference star characteristics in order to determine what characteristics produced the best reference stars.

3.1.2 Individual Reference Stars

First, I found the rms of the transit curves for each reference star individually, then sorted the individual reference stars by various characteristics which may or may not affect their value as reference stars. I selected the brightness of the reference star, as measured by counts at a given time and wavelength; spectral type, as determined by taking a χ^2 fit comparing the spectrum of the reference star and the spectrum of the target star; and proximity to the target star. I have plotted these sorted reference stars for the February 11th night of observations for

WASP 12 in Figures 3.2, 3.3, and 3.4, and for the July 1st night of observations for HD 189733 in Figures 3.5, 3.6, and 3.7.

3.1.3 Brightness

Figures 3.2 and 3.5 both show the rms of the transit curves produced by each individual reference star in order of brightness, with the brightest star on the far left and the dimmest star on the far right. The vertical blue line in each represents the brightness of the target star relative to the reference stars. Figure 3.2 shows that the brightness does not play a major role in determining the best reference stars, though there is a small increase in rms as brightness decreases when the reference stars are dimmer than the target star. Figure 3.5 shows that HD 189733 follows the same pattern, but the increase in rms is less prominent for HD 189733 than it had been for WASP 12. Both Figures 3.2 and 3.5 show that brightness is not a major concern when selecting reference stars for either WASP 12 or HD 189733.

3.1.4 Spectral Type

Reference stars with similar spectral types as my target star should produce better transit curves, since their spectra share many of the same spectral lines and peak at the same place. However, many of my reference stars have never been classified. This is especially true for those stars only listed in the Tycho Reference Catalogue. Therefore, instead of the actual spectral type, I used the χ^2 fit of the spectra of each of my reference stars to the spectrum of my target star as a proxy for stellar type. This will not give me information about exactly how the spectra differ, but it should allow me to find the reference stars with

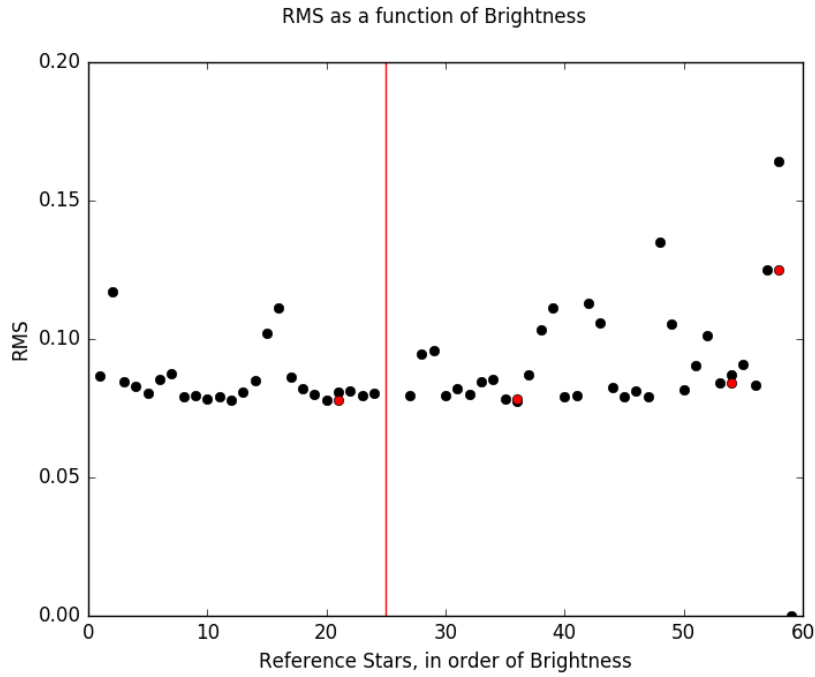


Figure 3.2: RMS for the transit curves produced by each individual reference star, sorted by brightness with brightness decreasing along the x axis, for WASP 12 (2/11/2016). The brightness of WASP 12 relative to the other stars is indicated by the vertical blue line, and the reference stars I ultimately selected are plotted in red.

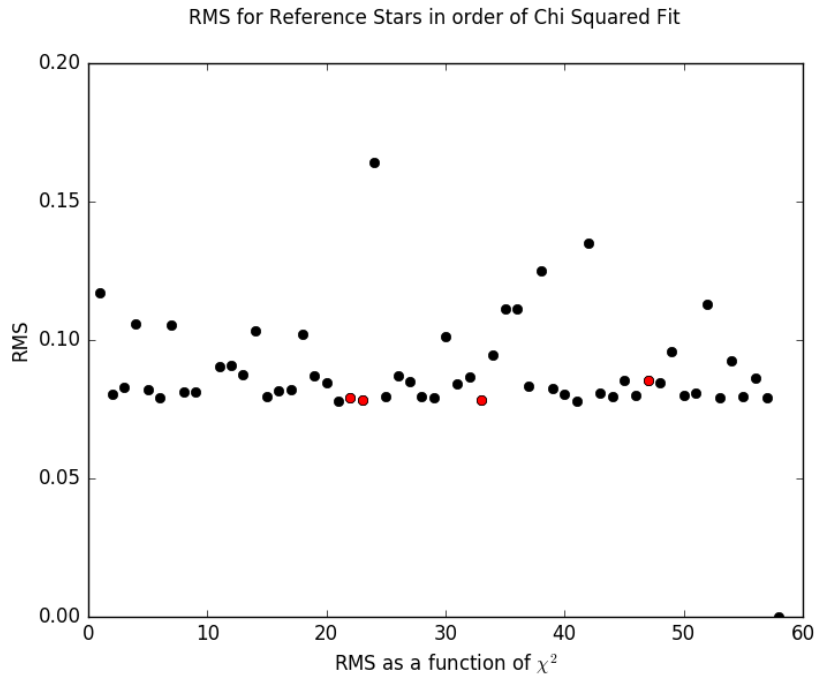


Figure 3.3: RMS for the transit curves produced by each individual reference star, sorted by spectral type with χ^2 increasing along the x axis, for WASP 12 (2/11/2016). The reference stars I ultimately selected are plotted in red.

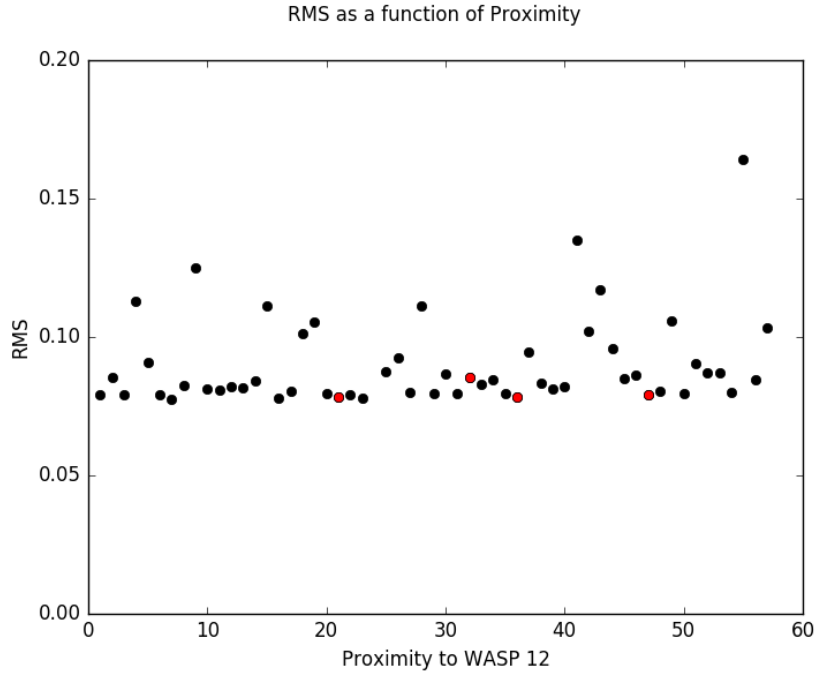


Figure 3.4: RMS for the transit curves produced by each individual reference star, sorted by proximity with separation increasing along the x axis, for WASP 12 (2/11/2016). The reference stars I ultimately selected are plotted in red.

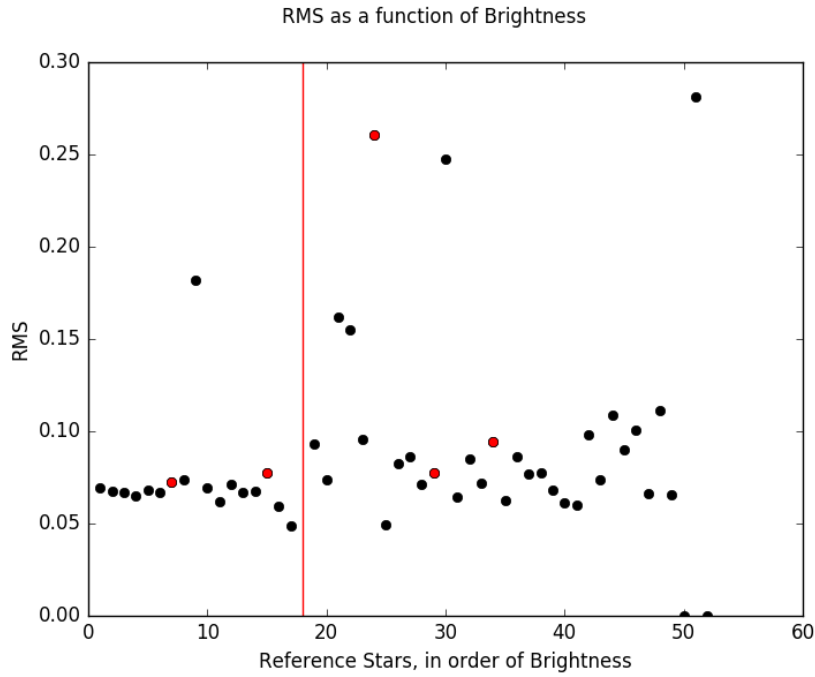


Figure 3.5: RMS for the transit curves produced by each individual reference star, sorted by brightness with brightness decreasing along the x axis, for HD 189733 (7/01/2016). The brightness of HD 189733 relative to the other stars is indicated by the vertical blue line, and the reference stars I ultimately selected are plotted in red.

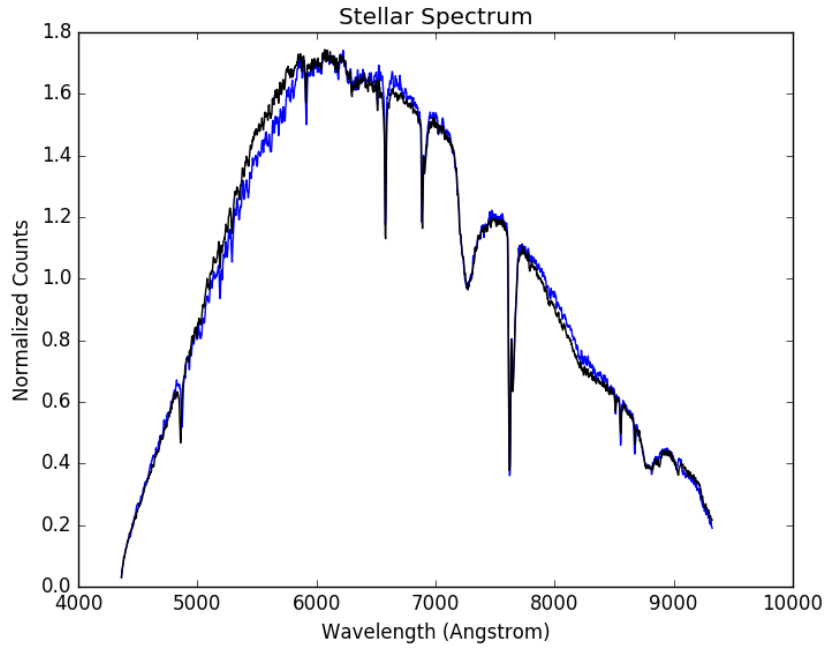


Figure 3.6: A reference star (TYC 1891-1014-1, spectral type unknown) whose spectrum (black) provides a low χ^2 fit when compared with the spectrum of WASP 12 (blue).

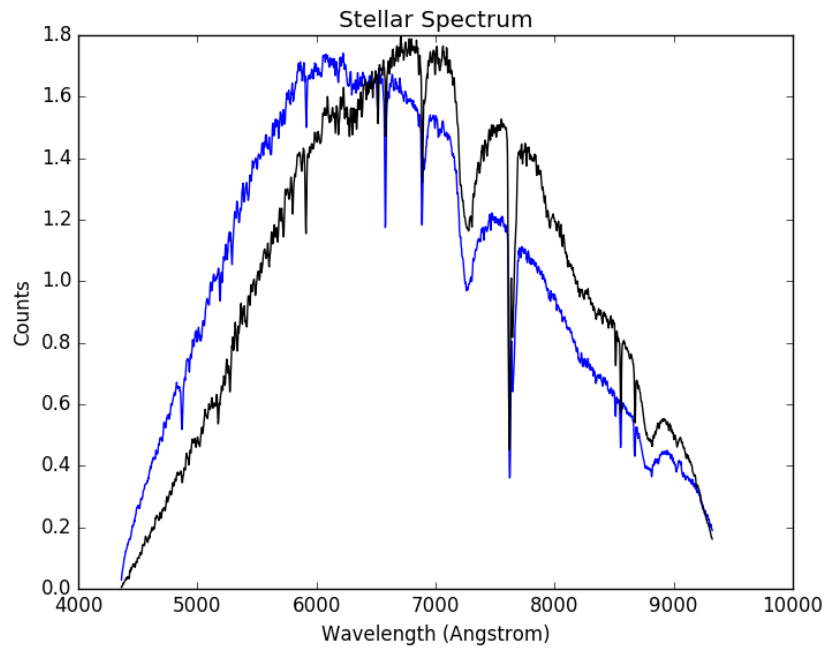


Figure 3.7: A reference star (TYC 1891-176-1, spectral type unknown) whose spectrum (black) provides a high χ^2 fit when compared with the spectrum of WASP 12 (blue).

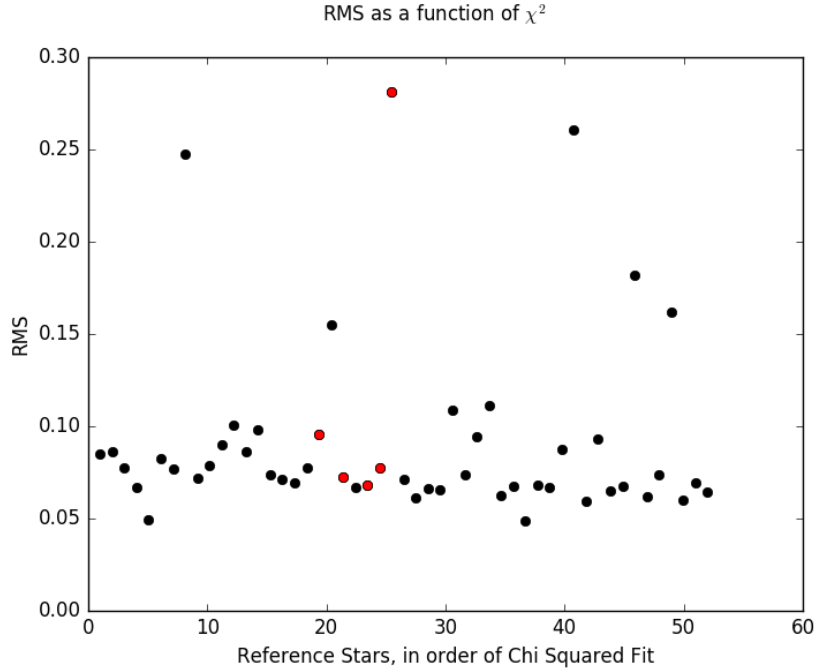


Figure 3.8: RMS for the transit curves produced by each individual reference star, sorted by spectral type with χ^2 increasing along the x axis, for HD 189733 (7/01/2016). The reference stars I ultimately selected are plotted in red.

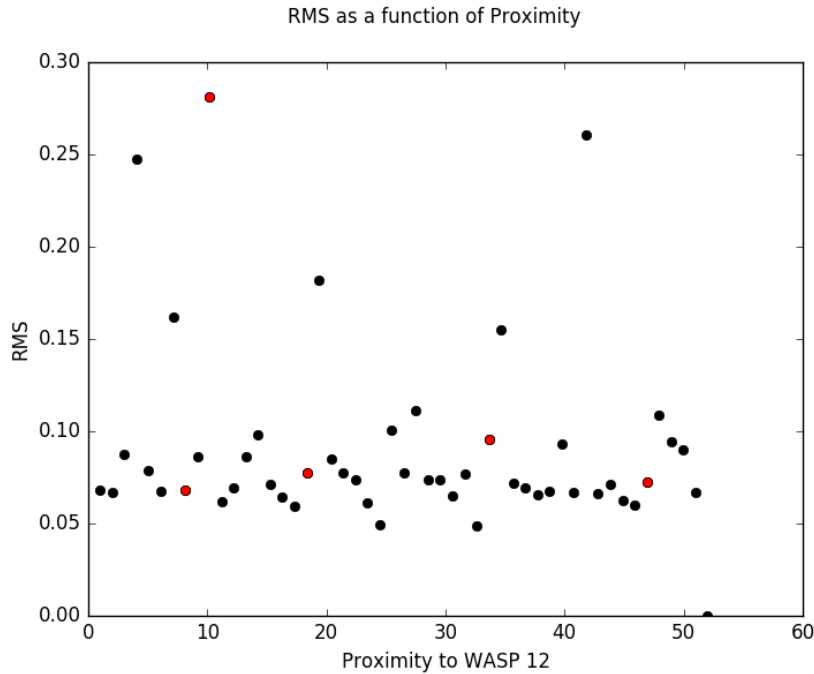


Figure 3.9: RMS for the transit curves produced by each individual reference star, sorted by proximity with separation increasing along the x axis, for HD 189733 (7/01/2016). The reference stars I ultimately selected are plotted in red.

the closest spectral types to my target star, since they will have the most similar spectra. I have included examples of stars with unknown spectral types which have a low χ^2 fit and a high χ^2 fit to the WASP 12 spectrum in Figures 3.6 and 3.7 for reference. Figure 3.6 shows a star whose spectral type is probably close to a G0V, due to its similarity to the WASP 12 spectrum. This is consistent with the Simbad B-V value for this star of 0.43 (compared to the WASP 12 Simbad B-V value of 5.7), as well as the lower J, H, and K band values relative to the B and V values. Meanwhile, the spectrum in Figure 3.7 is shifted into the red, which means that it probably comes from a star whose spectral type is later - maybe a K type star. This is consistent with the Simbad B-V value of 1.31, as well as the higher magnitude J, H, and K band values. Additionally, the spectrum of TYC 1891-176-1 in Figure 3.7 does not have the H_β spectral line, which indicates that its spectral type must be later than a G type.

Figures 3.3 and 3.8 show the rms of the transit curves produced by each individual reference star, sorted by the χ^2 fit of the spectrum of the reference star to the spectrum of the target star. In Figures 3.3 and 3.8, the reference stars whose spectra produce the lowest χ^2 fit to the spectrum of the target star are on the left and the reference stars with the highest χ^2 fit are on the right. Neither WASP 12 nor HD 189733 seem to have a correlation related to spectral type - the reference stars whose spectra match that of the target star do not appear to be better reference stars than those whose spectra do not match.

3.1.5 Proximity

Figures 3.4 and 3.9 show the rms of the transit curves produced by each individual reference star, sorted by proximity to the target star, calculated using

the `SkyCoords.separation` tool. Neither Figure 3.4 or Figure 3.9 show any particular correlation between proximity and rms, suggesting that proximity is not likely to correlate with the strength of the reference star.

3.1.6 Increasing Number of Reference Stars

Of the three reference star characteristics I examined in Figures 3.2, 3.3, 3.4, 3.5, 3.8, and 3.9, I found that rms does not seem to be a function of any of the characteristics I identified as possible indications of good reference stars.

My next step was to produce transit curves using an increasing number of reference stars, with the reference stars selected according to the same characteristics as before, namely, brightness, spectral type, and proximity. I additionally chose reference stars that had produced low rms initially, regardless of their other characteristics. I then plotted the rms of transit curves produced by these sets of reference stars simultaneously in Figures 3.10 and 3.11. Figure 3.10 represents the February 11th WASP 12 data, and Figure 3.11 represents the HD 189733 data. These figures allow me to directly compare the base rms of each of these characteristic sets, as well as the changing rms as more reference stars are added together.

Figure 3.10 shows the changing rms of each reference star characteristic as more reference stars are added to the set of reference stars. Adding together the best-fitting reference stars by individual rms causes the rms to rise well above the other characteristics, so it is not visible in Figure 3.10.

Of the other characteristics, spectral type and brightness produce the best rms as more reference stars are added. Brightness produces a roughly consistent rms as additional stars are added, whereas spectral type initially produces a very

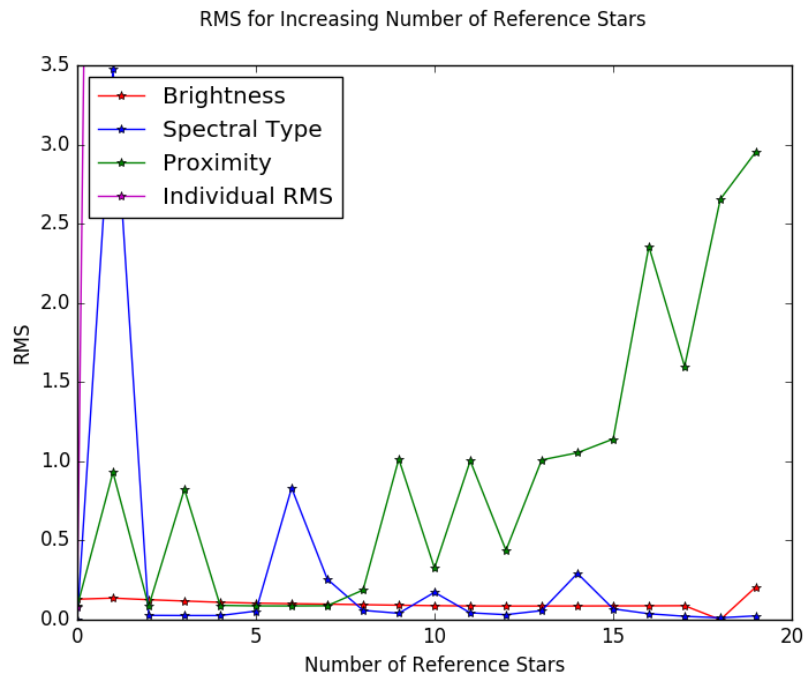


Figure 3.10: RMS for transit curves produced using an increasing number of reference stars for WASP 12 (2/11/2016).

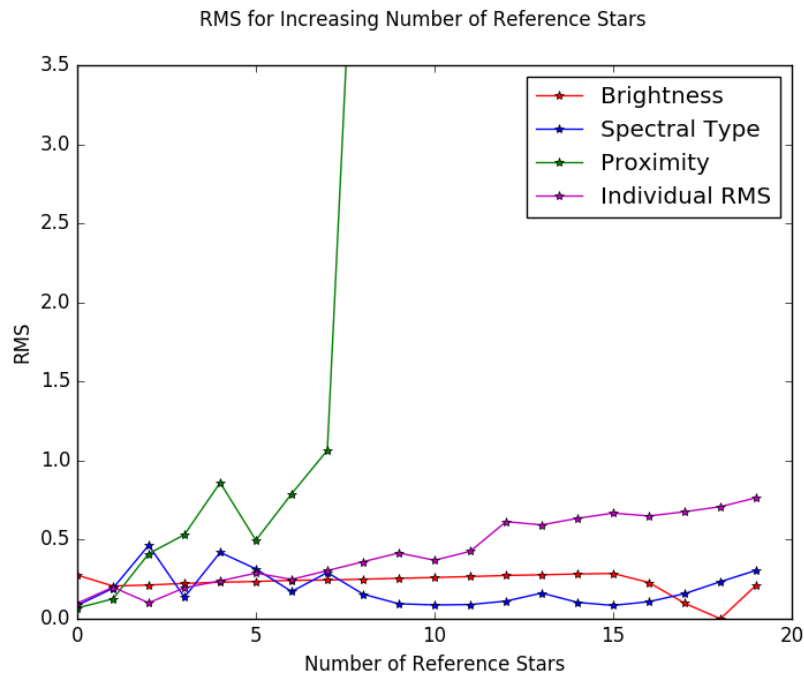


Figure 3.11: RMS for transit curves produced using an increasing number of reference stars for HD 189733 (7/01/2016).

large rms, but as additional stars are added, the rms decreases, until by the time I have added 20 reference stars, the rms produced by spectral type is slightly lower than brightness. Proximity and rms produce very large rms values, and these rms values increase as additional reference stars are added.

Figure 3.11 shows the changing rms of each reference star for the HD 189733 data. Like the WASP 12 data, Figure 3.11 shows that proximity and individual rms consistently produce the highest rms values, and increase as additional reference stars are added. Spectral type is again initially higher than brightness, but lowers with more reference stars, though this trend is less clear than it was for WASP 12.

3.1.7 Final Selections

After I gathered my sets of reference stars using the methods described above, I mixed all of the best reference stars in a variety of combinations looking for both minimum rms and the best possible transit curve. I have summarized the stellar properties of my final selections for each target star in Tables 3.1, 3.2, and 3.3, including the stellar properties of the target star for comparison, and I will additionally describe each selection in more detail.

Table 3.1: Final Selections for HD 189733

<i>Name</i>	<i>Spectral</i>	<i>V Mag</i>	<i>Right Angle</i>	<i>Declination</i>	<i>Separation</i>
	<i>Class</i>		<i>(J2000)</i>	<i>(J2000)</i>	<i>(arcseconds)</i>
HD 189733	K0V	7.67	20 00 43.1	+22 43 31	
HD 345470	A0V	10.81	20 00 29.41	+22 34 21.0	911.88
HD 189657	A0V	8.09	20 00 19.7	+22 26 28	2022.915
HD 345457	A5V	11.53	20 00 41.271	+22 51 20.41	1408.48
HD 345471	K7V	10.14	20 00 42.6538	+22 34 29.399	1507.13
TYC 2141-1110-1	...	11.07	20 00 02.967	+22 35 50.85	792.688

Table 3.2: Final Selections for WASP 12

<i>Name</i>	<i>Spectral Class</i>	<i>V Mag</i>	<i>Right Angle (J2000)</i>	<i>Declination (J2000)</i>	<i>Separation (arcseconds)</i>
WASP 12	G0V	11.69	06 30 32.794	+29 40 20.25	
TYC 1891-648-1	...	11.91	06 29 55.875	+29 50 19.85	768.47
TYC 1891-685-1	...	11.17	06 29 25.466	+29 34 18.24	949.6
TYC 1891-326-1	...	10.49	06 30 39.804	+29 37 40.39	654.4
HD 45784	F2V	8.11	06 30 45.616	+29 49 42.6	586.1

Table 3.3: Final Selections for GJ 3470

<i>Name</i>	<i>Spectral Class</i>	<i>V Mag</i>	<i>Right Angle (J2000)</i>	<i>Declination (J2000)</i>	<i>Separation (arcseconds)</i>
GJ 3470	M2V	12.27	07 59 06.2	+15 23 27	
2MASS J07594623+1538324	A0V	12.3	07 59 46.24	+15 38 32.4	1074.55
BD+161596	F5	9.50	07 58 13.2	+15 44 58	1501.055

For HD 189733, I selected HD 345470, HD 189657, HD 345457, HD 345471, and TYC 2141-1110-1, which produced an rms of 0.0708. All four were selected from the group rms by eye reference stars, and HD 345470 was additionally one of the closest stars in proximity to HD 189733.

For WASP 12, I chose four rms by eye stars, TYC 1891-648-1, TYC 1891-685-1, TYC 1891-326-1, and HD 45784, which produced an rms of 0.00988 for the February 11th observations and an rms of 0.125 for the February 12th ob-

servations. Some WASP 12 reference stars had the tendency to cause a spike in the February 11th midtransit, which would rise above the normalized flux of one, caused by a brief moment of cloud coverage which affected the reference and target stars differently. This spike would then contaminate the transit light curve sufficiently that my transit models would not find a transit at all. I therefore avoided these reference stars when making my selections.

For GJ 3470, I selected 2MASS J07594623+1538324 and BD+161596, both of which were selected from the group of rms by eye stars. These two reference stars produced an rms of 0.0207 for the January 13th observations.

3.2 Data Contamination

3.2.1 Binaries

Two of the three target stars, WASP 12 and HD 189733, are actually multiple star systems (Bechter et al. 2014). Neither are close binary systems, so both of the planets in question orbit only one of the two stars, while the second star is in a distant orbit. I do need to take care to avoid catching a transit of the second star during my observations, but since the second star is in a distant orbit, it should not interfere with my results.

3.2.2 Wind

I had some weather issues, but I tended to have either clear weather or weather which was sufficient to wash out the signal entirely. I lost one night of GJ 3470 data entirely and we lost the second half (post transit) of the other night of GJ 3470 data. I also see scatter due to wind throughout most of the February 12th

transit of WASP 12, which picked up about an hour into the observation and persisted through the entirety of the transit. The effect of wind in the data can be seen in Figure 3.1 earlier in this chapter, as well as in Figures 4.2 and 4.4 in Chapter 4.

3.2.3 Lost Data Points

Some data points were lost towards the end of the observations of some stars. Counts would spike exponentially upwards, reaching orders of magnitude greater than the rest of the night, and washing out the transit signal. This could have been due to scattering near the horizon, increased background light as dawn approached, or some other factor. This signature was present in the data of WASP 12 and GJ 3470, but not in the data for HD 189733. For the two stars affected, the signature was present in both nights of observations. I removed the spiking data points from the ends of the light curves, and luckily, never lost data during the transits.

3.2.4 Telluric Lines

Because we are observing from the ground, we do see interference in the transit signal when the light from the star interacts with the atmosphere of the Earth. This interaction produces telluric line contamination in the data. Molecules like water vapor, oxygen, ozone, and carbon dioxide produce especially strong signals in visible light, which is where my observations were taken. I have included a model of the telluric lines visible in my wavelength range, overlapping a spectrum of WASP 12, in Figure 3.12. The strongest telluric lines clearly match up with signatures in the spectrum of WASP 12. These signals can be corrected for,

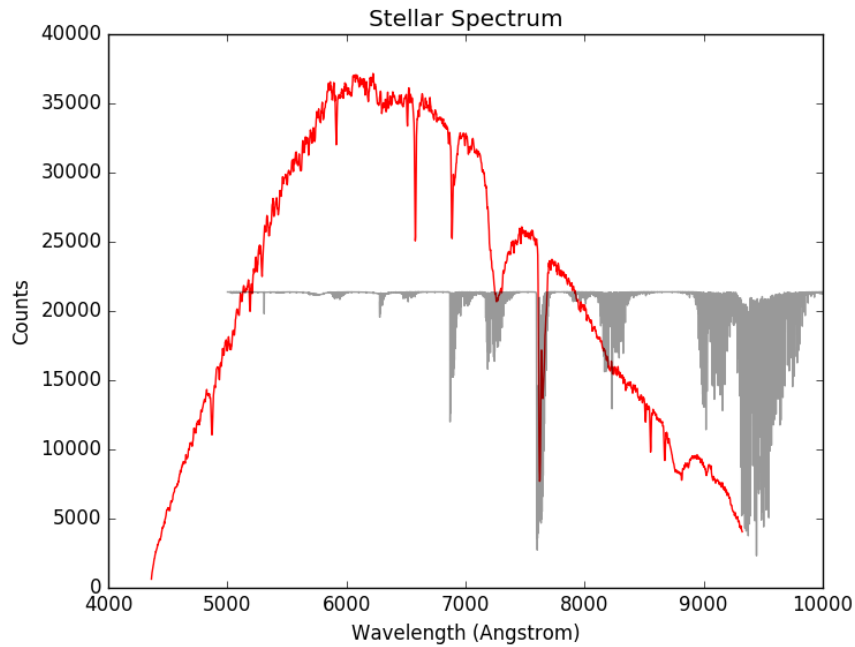


Figure 3.12: A model of the telluric lines in my wavelength range (grey) from Dr. Wilson Cauley overlaid over a spectrum of WASP 12 (red).

but since I am looking for a slope across my range of wavelengths rather than individual spectral signatures, I also had the option to simply identify and ignore the wavelengths at which these telluric lines occur in my final analysis. I will discuss this further in Chapter 5.

4 Analysis - White Light

4.1 General Method

4.1.1 Reduction

The instrument I used measures light received at 2,000 individual wavelength bins between 4000 Å and 9500 Å. The transmission of the various wavelengths changes depending on several loss mechanisms, including reflection at the end of the fiber path, fringing effects as the silicon of the CCD chip becomes transparent to redder light, and intrinsic properties of the fibers themselves. Therefore, individual wavelengths may not necessarily behave like the other wavelengths. I also expect the depth of the transit to differ across wavelengths due to the effect of Rayleigh scattering.

Rather than try to choose a wavelength or set of wavelengths to analyze first, I calculated the white light flux, that is, the sum of the light received in all wavelengths. I used the white light flux to develop a quick understanding of how the data behaves over the course of the night and of how easily detectable the transit is in general. This detectability varies for each wavelength, since the signal to noise of the data received over the course of the night will vary based on wavelength, but the white light transit is a good first indication of the systemic noise in the data.

I experimented with excluding some of the reddest light from my white light summation on the basis that the silicon used in the CCD detector can become

transparent to redder light, and therefore introduces diffraction effects into the redder light. The transmission of the fringed red light drops inconsistently at wavelengths above 8,500 Å, which may introduce error into the data. I therefore only included the light from 4500 Å to 8000 Å. The scatter in the HD 189733 data was not eliminated when I only used bluer light in my white light summations, indicating that the error introduced by this inconsistent transmission drop is not responsible for the scatter in the data.

Once I had white light rather than spectra for each star, I summed the white light from the reference stars and normalized both that sum and the flux from the target star to one. I divided the normalized flux from the summed reference stars from the normalized flux of the target star, and once again, normalized the resulting transit curve to one, producing Figures 4.1 and 4.2 for WASP 12, Figure 4.3 for HD 189733, and Figure 4.4 for GJ 3470. I use these white light transit curves to test and select reference stars to use for the wavelength dependent reduction later, as discussed in Chapter 3.

4.1.2 Modeling

After reducing the data, I used a linear, non-limb darkening model as a first-order tool to characterize the transit. By ignoring the limb darkening, I accept that the model I used will not accurately describe ingress and egress, the periods during which the planet is moving onto or off of the star, but it should accurately describe the depth of the transit. This linear model is based on the model developed by Mandel & Agol (2002) and follows the treatment given in Leiner (2010). For a more accurate description of ingress and egress, I later used a quadratic transit model by Kreidberg (2015), which I will describe later, which would take stellar

limb darkening into account. For now, since I am only interested in the transit depths at each wavelength, this simple model is sufficient.

The model depends on only one factor: the ratio of the radius of the planet to the radius of the star, as seen in Equation 1.2. The model then calculates the occulted light as a function of the impact parameter, which is itself a function of the time since the center of the transit. I used Equation 4.1 as follows:

$$\lambda^e(p, z) = \begin{cases} 0, & \text{if } 1 + p < z \\ \frac{1}{\pi}[p^2 K_0 + K_1 - \sqrt{4z^2 - (1 + z^2 - p^2)^2/4}], & \text{if } |1 - p| < z \leq |1 + p| \\ p^2, & \text{if } z \leq 1 - p \end{cases} \quad (4.1)$$

In equation 4.1, $\lambda^e(p, z)$ is the flux obscured by the planet (such that the total flux received by the observer is equal to $1 - \lambda^e(p, z)$), p is equal to the ratio R_p/R_s , z is the impact parameter as described above, and K_0 and K_1 are defined in Equations 4.2 and 4.3.

$$K_0 = \arccos\left(p^2 + z^2 + \frac{1}{2pz}\right) \quad (4.2)$$

$$K_1 = \arccos\left(1 - p^2 + \frac{z^2}{2z}\right) \quad (4.3)$$

Since the impact parameter z is a function of time since the center of the transit, I built transit models using these equations and inputting the ratio of the radii of the planet and star and an array of values for z which included the entire duration of the transit in hours.

In order to better fit the transits, I switched to using the Kreidberg (2015)

batman transit modeling code, and modeled my transits using a quadratic limb darkening model. Quadratic limb darkening introduces some variation in brightness across the face of the star, where the star is brightest at the center and dimmer towards the edge of the star. This phenomenon is called limb darkening, and occurs because we can look deeper into the stellar atmosphere when looking at the center of the star. The deeper part of the stellar atmosphere is hotter than the outer shells, which are what we see when we look at the edges of the stellar atmosphere, so the edges look darker than the center.

I used the `batman` transit modeling code to fit my transit curve to the data. I produced a transit curve for planets with a range of radii between 0% and 30% the radius of the star. I used the radii of the planets as my only variable parameter because the radius of the planet is directly related to the depth of the transit by Equation 1.2. I then subtracted the data from these transits, summed up the absolute values of the remainders, and chose the modelled transit which gave me the lowest total remainders, which would indicate that it was the modelled transit which best fit the data. I do not allow for the possibility of negative R_P/R_S values, which introduces a bias towards positive transit depths. However, negative transit depths are not physical results, so this should only affect cases where no real transit is present in the data.

For some nights of data, I only fit my transit model to a section of the data. For example, on February 12th, my data for WASP 12 has patches of data with much higher noise due to wind. When I fit my transit to that night of data, I ignore the patches contaminated by wind. Similarly, on February 12th, the data falls steadily over the course of the night. The data should instead lie on a straight line, since WASP 12 should not get dimmer over the course of the night. This could be due to poor tracking, contamination from WASP 12B, WASP 12A's

binary companion, or due to the fact that the atmosphere along our line of sight becomes thicker as we look closer to the horizon, and therefore, less light can get through as WASP 12 moves closer to the horizon, leading to a lower signal to noise. I only fit the data closest to the transit in order to minimize the effect of this slope on my modelled transit fit.

4.2 WASP 12

As a hot Jupiter with an extended or “inflated” atmosphere due to its close orbit around its star, WASP 12b has a transit depth of about 0.012, which is significant enough for me to clearly see a broadband transit in Figures 4.1 and 4.2. I have plotted in Figures 4.1 and 4.2 the modelled transit curve which best fits the data in red. I have also included the modelled transit curve produced by assuming a planetary radius corresponding to the accepted published value in blue for comparison. Figure 4.2 shows pockets of scatter before and during the transit due to increased wind at that point in time.

My modelled transit curves for February 11th fell slightly short of the expected transit depth. The February 11th shallow transits were not caused by the weather. Instead, they appear to be caused by issues with the longest and shortest wavelengths in my spectra, which I will discuss further in Chapter 5. These issues at some wavelengths are folded into my white light transit, and result in a transit depth of 0.0103, compared to the expected transit depth of 0.01216. However, the transit is clearly present, and when the wavelength issues are taken into account, is at a depth consistent with the expected depth.

Unlike my February 11th data, my modelled transit curves for February 12th were consistently only slightly deeper than the expected transit depth. However,

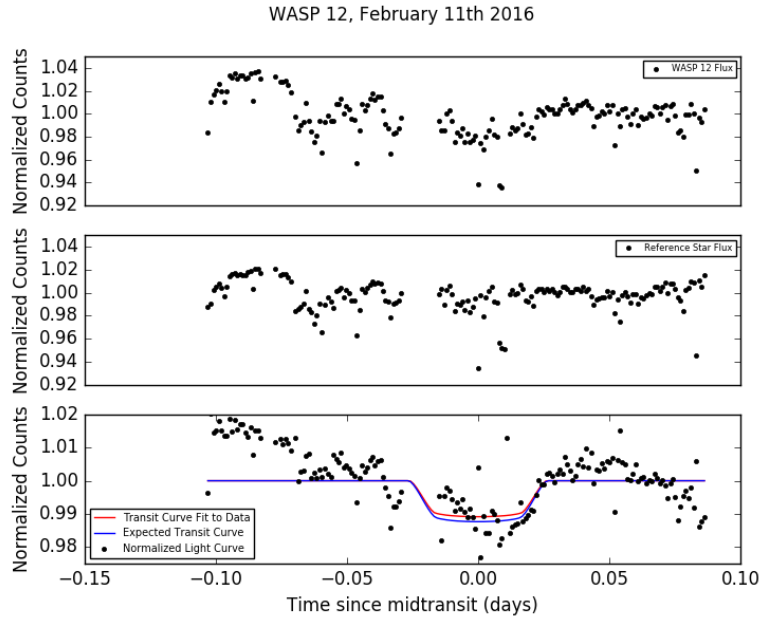


Figure 4.1: Relative flux of WASP 12 and the reference stars chosen for this observation on the night of February 11th, 2016, as well as the transit obtained from these fluxes. Included are the modelled transit curve which best fits the data (red) and the modelled transit curve produced by assuming a planetary radius corresponding to the accepted published value (blue).

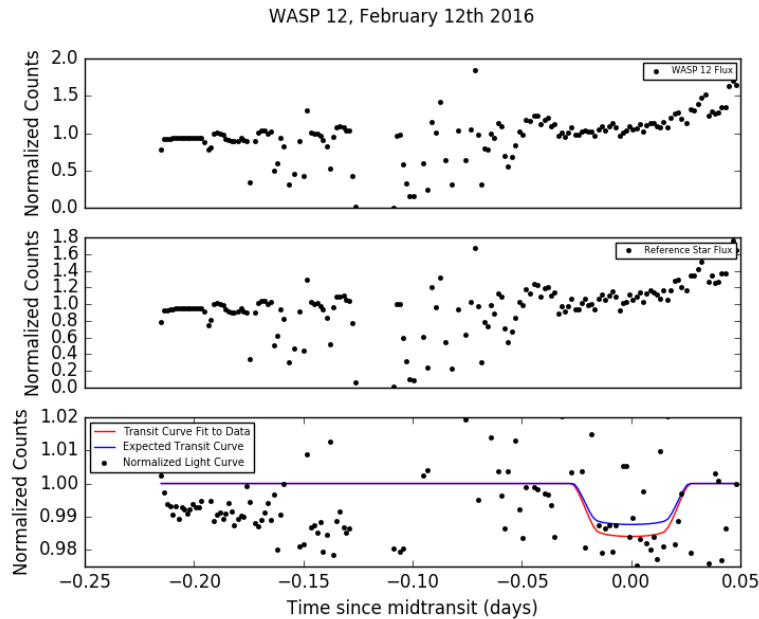


Figure 4.2: Relative flux of WASP 12 and the reference stars chosen for this observation on the night of February 12th, 2016, as well as the transit obtained from these fluxes. Included are the modelled transit curve which best fits the data (red) and the modelled transit curve produced by assuming a planetary radius corresponding to the accepted published value (blue).

as is clearly visible in Figure 4.2, the scatter of the data around the transit, caused by noise introduced by wind, is greater than the depth of the transit by a factor of three. This means that any transit detected is not significant, and cannot be used to make claims about the atmosphere of WASP 12b.

Although the February 12th observation of WASP 12 did not result in a significant transit detection, we do see that the data points prior to the increased wind that caused the scatter, up to about 0.15 days before midtransit, do have a low rms. These initial points suggest that the wind is the only reason why the February 12th data differ from the February 11th data, and demonstrate that weather is a major source of noise in these data sets, one which can completely obscure the transit.

4.3 HD 189733

Due to the brightness of the star, exposure times for the July 1st, 2016 observation were short, at 25 seconds, with readout times of 35 seconds between each observation. Atmospheric conditions were stable, with a few clouds and slight wind at points during the night which do not seem to affect the data. However, there is significant scatter even in the normalized white flux from HD 189733, as can be seen in Figure 4.3, and this scatter is also seen in the transit curve, which is completely washed out. The scatter is much larger than the Poisson errors, which give a signal to noise of 281, compared with the predicted signal to noise of 280. However, taking the average scatter in the transit curve of 0.15 as my average noise, compared to the average Poisson error in the transit curve of 6×10^{-5} , gives me a signal to noise of 0.1124, which indicates that the signal is completely lost in the scatter of the data.

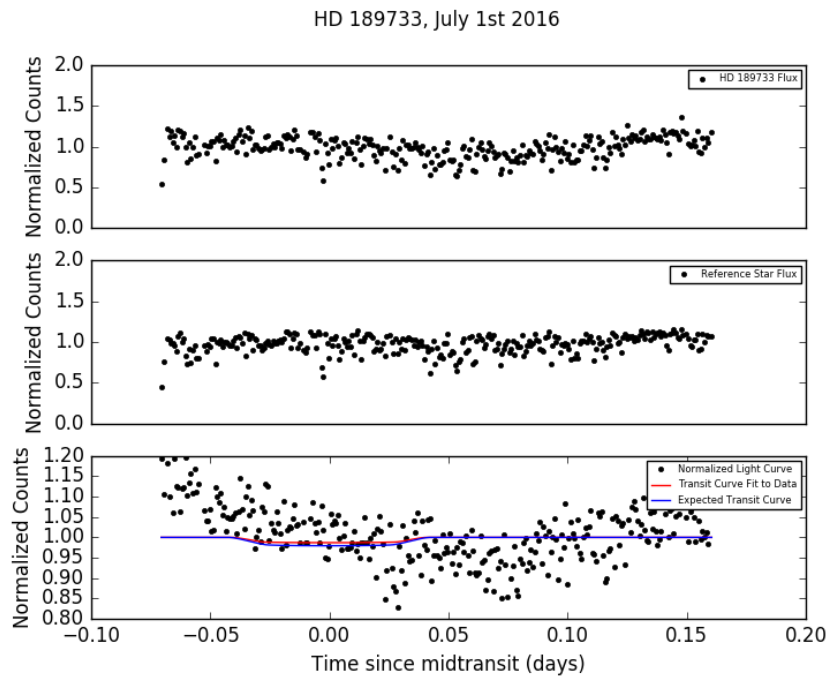


Figure 4.3: Relative flux of HD 189733 and the reference stars chosen for this observation on the night of July 1st, 2016 (see Chapter 2 for a list of reference stars), as well as the transit obtained from these fluxes. Included are the modelled transit curve which best fits the data (red) and the modelled transit curve produced by assuming a planetary radius corresponding to the accepted published value (blue).

4.4 GJ 3470

GJ 3470b, a warm Neptune, is among the smallest exoplanets with a confirmed Rayleigh Scattering detection (Dragomir et al. 2015). Unfortunately, this means that its transit depth is more shallow than the transit depths of WASP 12b and HD 189733b, at only 0.0057 (Nascimbeni et al. 2013). Additionally, its star has a low V-band brightness at 12.3 mag (Biddle et al. 2014), which will further reduce our signal to noise. I ultimately found a signal to noise ratio of 21, which means that the transit of GJ 3470b will be difficult, if not impossible, to detect, even in the best conditions.

While both nights of data were affected by bad weather, the weather issues on January 13th observation did not begin until after the transit. However, the scatter in the data from that observation was still about five times greater than the transit depth, as seen in Figure 4.4. Therefore, the measured transit depths vary wildly, and cannot be counted as a significant transit detection.

Ultimately, I was only able to detect a whiteflux transit in one out of six observations. The other nights were plagued by bad weather and instrumental issues, such as the issues causing the scatter in the light curve of HD 189733. The biggest issue I found when producing my whiteflux transits was the weather, which is clearly a major issue when it comes to producing a clean, significant transit detection.

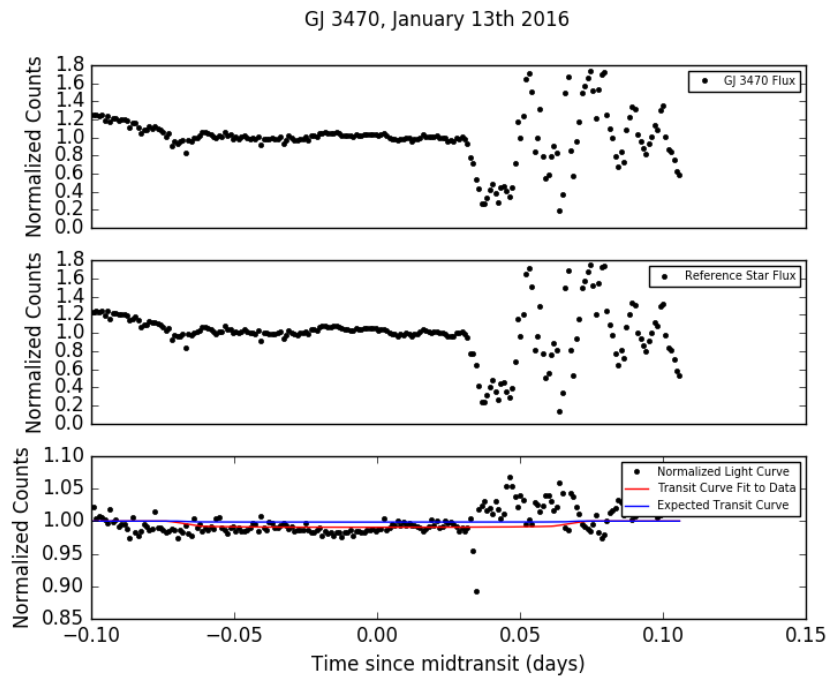


Figure 4.4: Relative flux of GJ 3470 and the reference stars chosen for this observation on the night of January 13th, 2016 (see Chapter 2 for a list of reference stars), as well as the transit obtained from these fluxes. Included are the modelled transit curve which best fits the data (red) and the modelled transit curve produced by assuming a planetary radius corresponding to the accepted published value (blue).

5 Analysis - Spectra

5.1 Transit Detection

5.1.1 Wavelength Dependence

Once I had a light curve for white light, I used the same process with the spectrally separated light. I found normalized transit light curves for each wavelength and fit modelled transits to the light curves at every wavelength. I plotted the transit depths and the ratio of the radius of the planet and the radius of the star for each wavelength in Figures 5.1 — 5.5 for the observations of WASP 12, HD 189733, and GJ 3470, respectively.

5.1.2 Rayleigh Scattering

I fit my data with a simple scattering model, following Stevenson et al. (2014a) and Sing et al. (2013), where the slope of the transmission spectrum is related to temperature by the power law in Equation 5.1:

$$\frac{d(\frac{R_P}{R_S})}{d\ln(\lambda)} = \alpha H = \frac{\alpha k T}{\mu g}, \quad (5.1)$$

where H is the atmospheric pressure scale height, R_P is the radius of the planet, R_S is the radius of the star, λ is wavelength, T is the temperature of the atmosphere of the planet, k is the Boltzmann constant, μ is the mean molecular weight, g is the surface gravity of the planet, and α is the index of the power law.

To model a Rayleigh scattering dominated transmission spectrum for WASP 12, I used a temperature of 1870K, a surface gravity of 2.99 dex, and a mean molecular weight of 2.3 g mol^{-1} , following Stevenson et al. (2014a) and Hebb et al. (2009). I also used an α of -4 , which corresponds to scattering dominated by Rayleigh scattering. I used this slope, along with the fixed R_P/R_S value at $4,500 \text{ \AA}$ of 0.119, following Sing et al. (2013), in Figures 5.1 and 5.2 to indicate the line along which we expect our transmission spectrum to fall.

5.2 Analysis of Transit Detections

5.2.1 WASP 12

When I plot the transit depths at each wavelength for the February 11th observation of WASP 12 in Figure 5.1, the transmission spectrum is dominated by contaminating spectral signatures, which drown out any Rayleigh scattering slope. I have identified each signature in Figure 5.2. I have been able to identify the source of several of these signatures. My goal is to be able to either remove these signatures from the data or avoid them in future observations.

The first and second signatures are the increased scatter between 4300–5000 \AA and between 8000–9000 \AA . The scatter is caused by a loss of signal to noise at the edges of the blaze function, where less light is detected in general. The loss of signal here drives an increase in scatter in the data at both edges of the transmission spectrum, as seen in Figure 5.1. This effect cannot be removed from the data.

The second blaze function signature is affected more strongly by scatter than the first, due to the presence of an additional third signature. This signature is caused by inconsistent transmission loss after 8500 \AA , potentially caused by

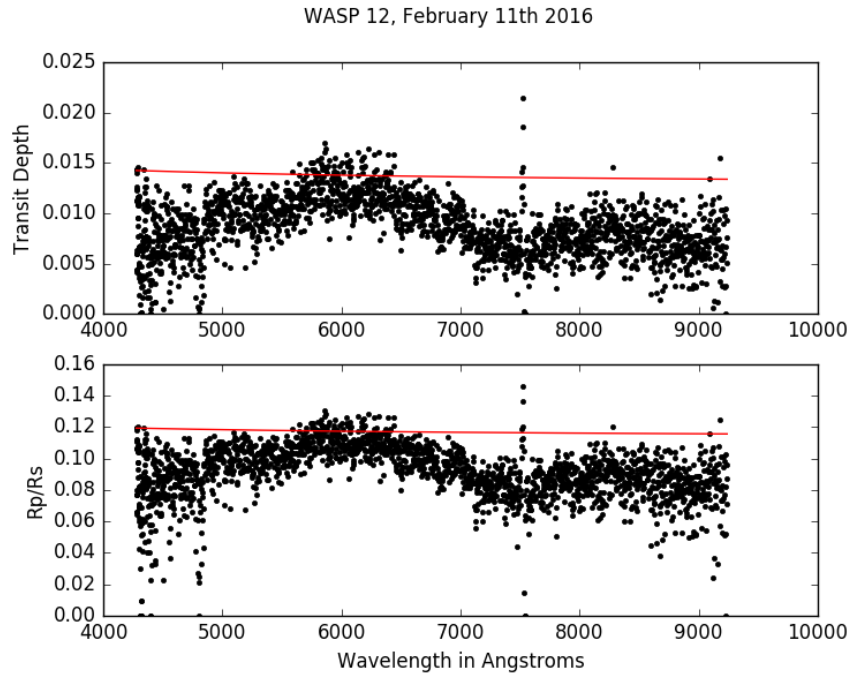


Figure 5.1: Unbinned transit depth and the ratio of the radius of the planet to the radius of the star vs wavelength. The red line represents the expected Rayleigh scattering transmission spectrum.

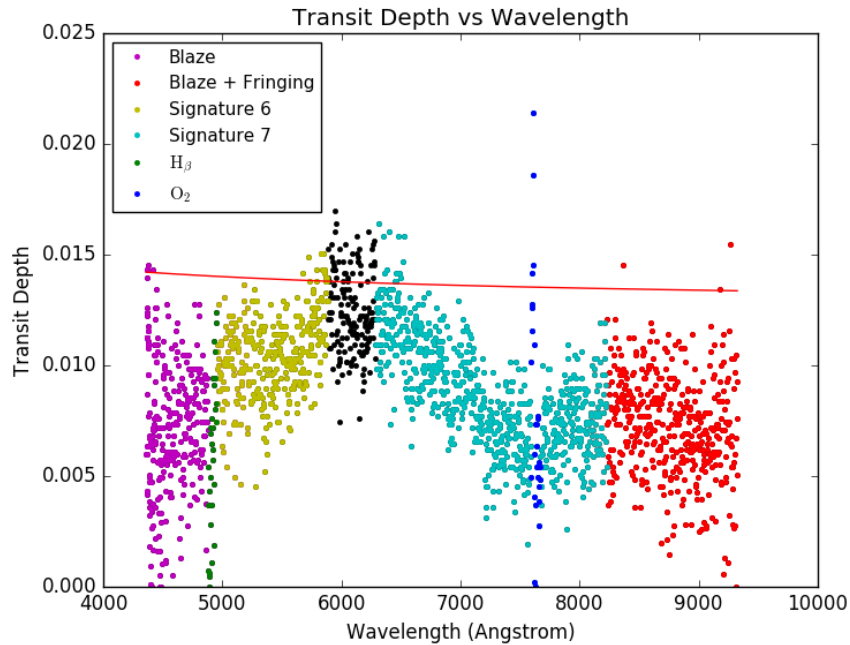


Figure 5.2: Unbinned transit depth and the ratio of the radius of the planet to the radius of the star vs wavelength. The red line represents the expected Rayleigh scattering transmission spectrum.

fringing, or the increased transparency of the silicon in the CCD chip to the reddest light in our wavelength range. This introduces additional scatter, increasing with wavelength after the transition point of 8500 Å. The red edge blaze function is difficult to untangle from fringing effects, so while both are present in this spectrum, it is not possible to determine exactly how strong the effect of either signature individually really is.

Like the second signature, the first signature is also further contaminated by another signature. This fourth signature is an H_β spectral line at 4861 Å. H_β is a prominent line in most stellar spectra, especially in the spectra of larger stars, such as WASP 12. Moreover, it lies in the edges of the blaze function, further exaggerating the effect it has on the transmission spectrum. The result is a deep but narrow spectral feature, which does not affect a significant portion of wavelength space and therefore does not negatively affect the Rayleigh scattering signature.

The fifth signature is another narrow line, this time caused by an O_2 telluric line in the Earth's atmosphere. Because it is a telluric signature rather than a stellar spectral signature, it causes both a narrow peak and drop in the transmission spectrum. Like the H_β signature, the O_2 telluric signature affects a small portion of wavelength space, and does not significantly affect the Rayleigh scattering signature.

While I have not yet been able to identify the sources of the sixth and seventh signatures, I have been able to characterize their effects on the transmission spectrum.

The sixth signature lies roughly between 5000–6000 Å, and causes a broad dip in the transmission spectrum. Since it overlaps with the first signature, the exact wavelength range affected by this sixth signature is difficult to define. This sixth

signature also makes it difficult to remove the first signature from the data, since it hinders our ability to determine where the first signature ends. The seventh signature behaves similarly to the sixth, but lies roughly between 6500–8000 Å. The seventh signature overlaps with the second and third signatures, making it difficult to remove them from the data. Neither the sixth nor the seventh signatures can be characterized well enough to model them and remove the model from the data, and their interactions with the other signatures inhibit my ability to safely remove those signatures, as well. Moreover, I do not know the cause of the signatures, so even if I could remove them from the transmission spectrum, I would not be sure that they were, in fact, instrumental rather than real signatures in the transmission spectrum.

Of the signatures identified, the two narrow lines are the least problematic. They do not affect a broad range of wavelengths, and therefore do not affect the Rayleigh scattering slope. The two blaze function edge effect signatures could potentially be modeled and removed from the data, but are inherent to the observed flux, and therefore cannot be avoided in future observations. The third signature arises due to the behavior of the silicon in the CCD chip at wavelengths above 8500 Å, and therefore can be avoided in future observations by shifting our wavelength range such that we avoid wavelength over 8500 Å.

The sixth and seventh features pose a more difficult problem. These signatures do not seem to be connected to any real signatures in either the planet or the Earth’s atmosphere, and are therefore probably instrumental, but the cause of the signatures has not yet been determined. I cannot model them and remove the signature from the data, because they overlap with other signatures and cannot be properly characterized. I also cannot avoid them without knowing what causes them, but these signatures are both broad, and the seventh signature is one of the

deepest signatures, which means that they dominate the transmission spectrum in their wavelength ranges.

5.3 Analysis of Transit Non-Detections

While I only detected a transit for the February 11th observation of WASP 12, I was able to create transmission spectra for the non-detection observations of HD 189733, GJ 3470, and the February 12th observation of WASP 12. These transmission spectra may be able to provide insight into why we failed to detect a transit, which will allow me to better understand what conditions to avoid in future observations.

5.3.1 WASP 12

The February 12th observation of WASP 12 produced the transmission spectrum in Figure 5.3. This observation did not produce a consistent or believable transit, since the scatter in the data is greater than the transit depth, which means the transit depths detected are not true transit depths. However, we can see several identifiable signatures in the data. I see the same O₂ telluric line as in the February 11th observation of WASP 12, as well as two broader features at 6740 Å and 7000 Å which correspond with other telluric lines, but which are much broader than the O₂ line. I do see scatter associated with the blaze function on the blue edge, but the red edge lacks the scatter associated with either the blaze function or fringing effects. Instead, the red edge is characterized by a steep rise in transit depth, potentially due to the transit occurring late in the observation, risking the effects of pre-dawn twilight.

I do not see any signs of Rayleigh scattering, or any other atmospheric sig-

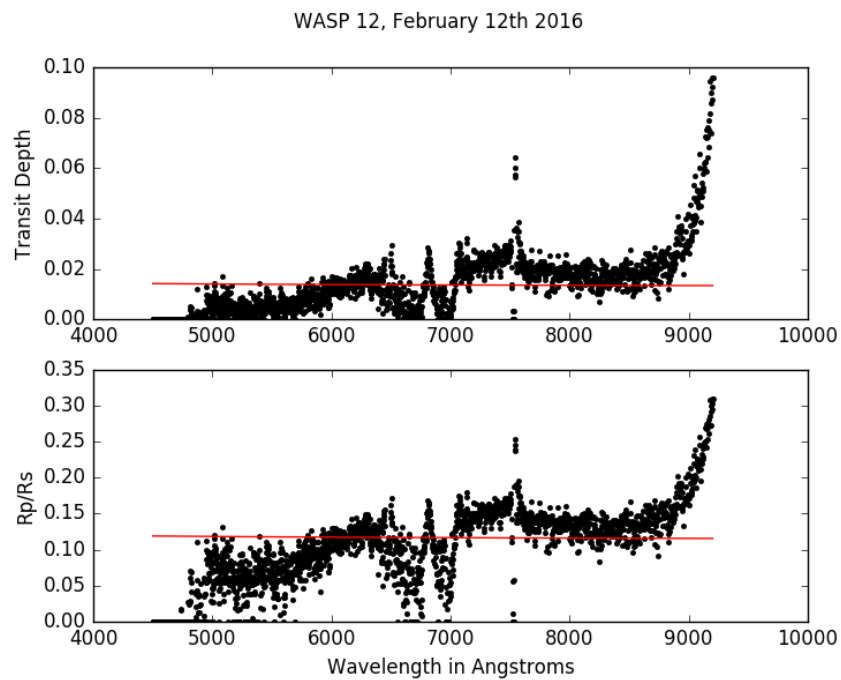


Figure 5.3: Unbinned transit depth (fit by `batman` code in data without a detected transit) and the ratio of the radius of the planet to the radius of the star vs wavelength for the observations of WASP 12 taken on February 12th, 2016. The red line represents the expected Rayleigh scattering transmission spectrum.

natures, in this observation of WASP 12. The signatures I do see are related to systemic and weather issues, and the weather issues dominate. I would not expect any signatures from the planet to be present in this transmission spectrum, since the scatter in the data interferes with my ability to measure the transit depths.

5.3.2 HD 189733

My observation of HD 189733 resulted in the transit spectrum in Figure 5.4, with the red line representing the expected Rayleigh scattering slope as calculated by McCullough et al. (2014). My batman model fitting procedure consistently detected a transit, but at much greater depths than is expected or realistic. The depths rise rapidly as wavelengths decrease. I do not see signs of blaze function scatter on the blue edge, but there is increased scatter on the red edge. This scatter could be either due to the blaze function or to fringing effects, and it is not possible to determine which is the real cause.

Both HD 189733 and the February 12th observation of WASP 12 have transit depths of zero at the shortest wavelengths. While the zero depth follows a steady decrease for WASP 12, the transit depths for HD 189733 drop suddenly to zero following a rapid, extensive increase in transit depths as wavelength decreased.

5.3.3 GJ 3470

I was able to produce a transmission spectrum for the January 13th observation of GJ 3470, as seen in Figure 5.5, but not for the January 3rd observation, due to weather effects. The red Rayleigh scattering slope in Figure 5.5 is the expected Rayleigh scattering signature as calculated by Awiphan et al. (2016). Figure 5.5 shows that while my code may find that a transit is the best fit, the depths are

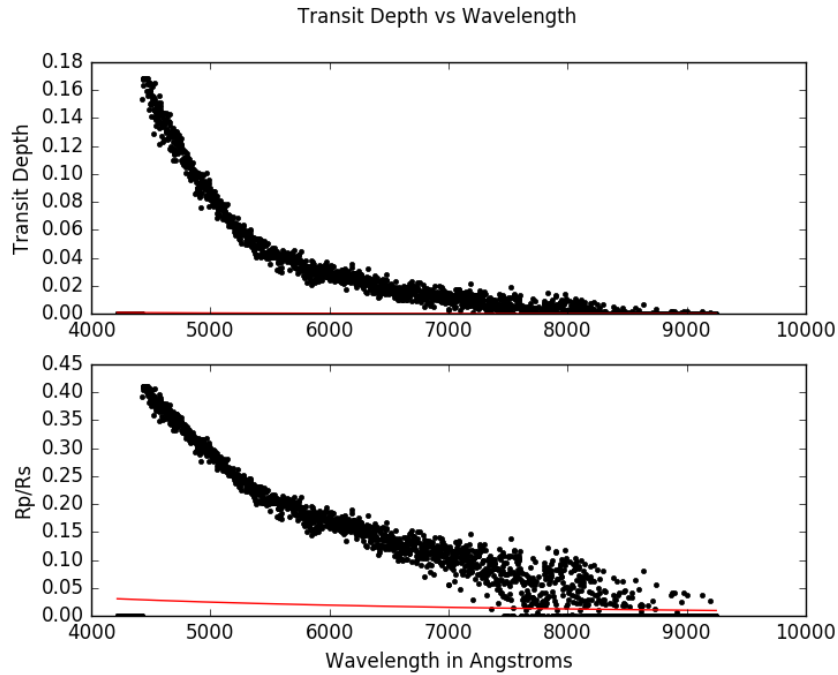


Figure 5.4: Transit depth (fit by `batman` code in data without a detected transit) and the ratio of the radius of the planet to the radius of the star vs Wavelength for the observations of HD 189733 taken on July 1st, 2016.

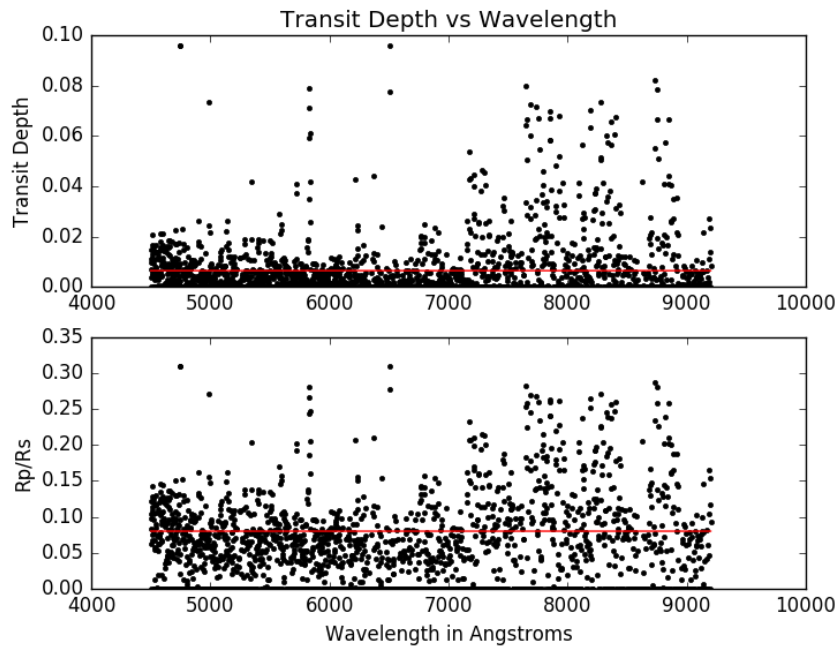


Figure 5.5: Transit depth (fit by `batman` code in data without a detected transit) and the ratio of the radius of the planet to the radius of the star vs Wavelength for the observations of GJ 3470 taken on January 13th, 2016.

consistent with random noise, and do not fit the expected Rayleigh scattering slope. There are no weather or systemic signatures in this transmission spectrum, indicating that the transit depths are not real detections.

6 Summary and Conclusions

6.1 Instrumentation

My attempt at exoplanet atmosphere detection with the WIYN telescope was exploratory, and while I did not detect the feature I set out to detect, the data I was able to collect can still help me better understand the limitations of the telescope moving forward. Both my non-detections and my one successful transit detection can provide insight into the telescope and the observational set-up used.

6.1.1 Transit Detection

Out of six scheduled nights of observations, I was able to detect a transit on one of the six nights. We were able to open the telescope on five out of the six nights, but weather effects dominated two other nights of data, instrumental issues dominated another, and the signal to noise of a fourth was not sufficient to detect the shallow GJ 3470b transit. Out of six possible observations, I was only able to detect one transit.

I found that the WIYN telescope is only sensitive to hot Jupiters like WASP 12b or HD 189733b, and is not sensitive enough to detect warm Neptunes like GJ 3470b. Since the star GJ 3470 is an M2 star, any other smaller planets are not likely to have a more favorable R_p/R_s ratio, which means that any planets of comparable size or smaller, such as Super-Earths or rocky planets will not be detectable by the WIYN telescope.

6.1.2 Transmission Spectrum

The Hydra bench spectrometer was not designed for the study of exoplanet atmospheres, and its abilities are not necessarily ideal for this study. For example, although the multi-object spectrometer observes fifty to sixty reference stars, I found that using three or four reference stars resulted in a better transit curve than using the full set, and that variance in the light that fell on each fiber could easily result in reference stars shifted in wavelength relative to one another if my wavelength calibrations were even slightly off. The extent of the blaze function inherent to the Hydra spectrometer created significant instrumental scatter, which shrunk my useable wavelength space by a couple thousand Ångstroms, which is about a third of my overall spectrum.

Despite the limitations of the Hydra bench spectrometer, I did successfully detect a transit at all wavelengths for WASP 12. With a better understanding of the instrumental issues, a future transmission spectrum could potentially detect a signature such as Rayleigh scattering. More sensitive work, however, such as molecule detection, is probably not feasible with this instrument.

6.1.3 Ground Based Telescopes

Although half of my planned nights of observations were either lost due to or contaminated by bad weather, I was able to observe unhindered by weather on the other three nights. The bad weather was not seasonal. Of three sets of two consecutive observations occurring in January, February, and July, all of 2016, each lost one and only one night of data. Therefore, in future attempts to use a ground-based telescope for exoplanet atmospheric studies, I would anticipate losing half of the planned nights of data, and asking for twice as many transits as

are actually needed.

Furthermore, telluric interference did not pose a significant problem to my data set. The major telluric line present in my transmission spectrum was narrow and obvious, and would not have interfered with the Rayleigh scattering signature had I detected it. Telluric interference is the most potentially damaging problem with ground-based observing as compared to space-based observing, but it did not pose a problem for the broad, prominent Rayleigh scattering signature. More detailed signatures, such as molecular bands, may need to take more care with telluric interference, but this interference will probably be able to be removed from the data if necessary.

6.2 Future Work

With a better understanding of the WIYN telescope and the Hydra bench spectrometer, future observations can begin to look for ways to improve the instrumental set-up. Currently, the most pressing question to ask is whether the WIYN telescope is likely to be a valuable tool in future exoplanet atmosphere studies.

6.2.1 Potential Improvements

There remain unidentified instrumental issues, including the scatter in the light curve of HD 189733 and the major signatures in the transmission spectrum of WASP 12. These instrumental issues dominate the signatures, preventing a transit detection in HD 189733 and contaminating the transmission spectrum for WASP 12. While these instrumental issues remain unidentified, I cannot remove their signatures from the data or avoid encountering the issues in future observations.

However, they are not necessarily unavoidable - only HD 189733 showed signs of greatly increased scatter, and while I only have a planetary transmission spectrum from one observation of WASP 12, I do not see signs of this instrumental signature in the transmission spectra of the other observations. Unless this signature proves to be planetary in origin, this suggests that the signature is not present in all data sets. Therefore, while I cannot identify these two signatures and do not know what causes them, I do think they could potentially be avoidable if I am able in the future to identify the cause of the signatures.

6.2.2 Value of Future Attempts

I attempted to observe Rayleigh scattering in the atmospheres of WASP 12b, HD 189733b, and GJ 3470b in large part as a means of evaluating the potential value of the Hydra spectrometer on the WIYN telescope as a tool for the study of exoplanet atmospheres. I did not detect Rayleigh scattering in any of the planets I observed, but I was still able to gain a better sense of this potential value.

I did successfully detect a transit and a transmission spectrum for WASP 12, although instrumental issues dominated that spectrum and washed out the Rayleigh scattering signature. I found that while the Hydra bench spectrometer is not ideally designed for the study of exoplanet atmospheres, the system is sensitive to atmospheric signatures on the scale of Rayleigh scattering, though probably not sensitive to less prominent atmospheric signatures such as molecular features. Therefore, the potential value of the WIYN telescope in the case of exoplanet atmospheres is limited to a small set of particularly prominent features.

The WIYN telescope, and the Hydra bench spectrometer, were not designed for the study of exoplanet atmospheres, and therefore impose limitations on our

ability to use them for this purpose. While I do think we could use this set-up for very limited atmospheric detections, I do not think we could extend this use to more detailed studies. Because other telescopes can detect the same signatures I could detect with the WIYN telescope, such as Rayleigh scattering and other prominent scattering features, with greater ease and with the sensitivity to additionally detect molecular features simultaneously, I do not think that the WIYN telescope will play a major role in future exoplanet atmospheric studies. However, the instrumental understanding gained in this project could inform the design of future ground-based observations in the future.

6.3 Conclusions

As we begin to better understand the context in which our planet Earth exists, we can begin to pursue an understanding of the context in which we, as intelligent life, exist. Our first glimpses into the wide scope of planetary possibilities has already proven surprising, with many new types of planets that do not exist in our Solar System, and that we therefore did not know existed thirty years ago. Our discoveries of hot Jupiters, Super-Earths, and massive, distant planets all suggest that the universe is full of more planetary diversity than we could imagine. As our sample of these new and exciting planets increases, it is our job to study and characterize each planet as well as possible. The more planets we can study and understand, the more likely we will be to discover the kinds of patterns and populations that could lead to a new way of thinking about our place in the universe.

The study of exoplanet atmospheres is currently in its infancy, but already we have made astonishing progress. From lava planets to water worlds, we have

been able to redefine what planetary conditions could exist. But with tens of thousands of known exoplanets waiting to be studied, we need to use our resources thoughtfully. Billion dollar space telescopes may be the best tools for the job, but if we can use their younger, ground-based cousins as well, we can massively increase our ability to study these exciting new planets. My attempt to use the WIYN telescope may not have succeeded, but the idea of using ground-based telescopes for exoplanetary atmosphere study has succeeded in the past, and as we continue to explore our rapidly expanding pool of exoplanets, ground-based telescopes will play an increasingly vital role.

Bibliography

Agúndez, M., Parmentier, V., Venot, O., Hersant, F., & Selsis, F. 2014, *AAP*, 564, A73

Angerhausen, D., et al. 2015, *Journal of Astronomical Telescopes, Instruments, and Systems*, 1, 034002

Awiphan, S., et al. 2016, *MNRAS*, 463, 2574

Barden, S., Armandroff, T., Willmarth, D., & Glaspey, J. 2009, *WIYN HYDRA AND BENCH SPECTROGRAPH USERS MANUAL - v6* (National Optical Astronomy Observatory)

Bechter, E. B., et al. 2014, *APJ*, 788, 2

Benneke, B., & Seager, S. 2012, *APJ*, 753, 100

Bétrémieux, Y. 2016, *MNRAS*, 456, 4051

Biddle, L. I., et al. 2014, *MNRAS*, 443, 1810

Bisikalo, D. V., Kaigorodov, P. V., & Konstantinova, N. I. 2015, *Astronomy Reports*, 59, 829

Burton, J. R., Watson, C. A., Rodríguez-Gil, P., Skillen, I., Littlefair, S. P., Dhillon, S., & Pollacco, D. 2015, *Mnras*, 446, 1071

Chan, T., Ingemyr, M., Winn, J. N., Holman, M. J., Sanchis-Ojeda, R., Esquerdo, G., & Everett, M. 2011, *Aj*, 141, 179

Clark, R. N., et al. 2014, AGU Fall Meeting Abstracts

Copperwheat, C. M., et al. 2013, MNRAS, 434, 661

Crossfield, I. J. M., Barman, T., Hansen, B. M. S., & Howard, A. W. 2013, AAP, 559, A33

Di Gloria, E., Snellen, I. A. G., & Albrecht, S. 2015, AAP, 580, A84

Dragomir, D., Benneke, B., Pearson, K. A., Crossfield, I. J. M., Eastman, J., Barman, T., & Biddle, L. I. 2015, APJ

Ehrenreich, D., et al. 2014, AAP, 570, A89

Fukui, A., et al. 2013, APJ, 770, 95

Hebb, L., et al. 2009, APJ, 693, 1920

Jensen, A. G., Redfield, S., Endl, M., Cochran, W. D., Koesterke, L., & Barman, T. 2012, APJ, 751, 86

Jordán, A., et al. 2013, APJ, 778, 184

Khalafinejad, S., & Hoeijmakers, J. 2015, IAU General Assembly, 22, 2255364

Kirk, J., Wheatley, P. J., Loudon, T., Doyle, A. P., Skillen, I., McCormac, J., Irwin, P. G. J., & Karjalainen, R. 2016a, ArXiv e-prints

Kirk, J., Wheatley, P. J., Loudon, T., Littlefair, S. P., Copperwheat, C. M., Armstrong, D. J., Marsh, T. R., & Dhillon, V. S. 2016b, MNRAS

Kreidberg, L. 2015, PASP, 127, 1161

Leiner, E. 2010, Master's thesis, Wesleyan University

- Mandel, K., & Agol, E. 2002, APJL, 580, L171
- Mandell, A. M., Haynes, K., Sinukoff, E., Madhusudhan, N., Burrows, A., & Deming, D. 2013, APJ, 779, 128
- Mayor, M., & Queloz, D. 1995, Nature, 378, 355
- McCullough, P. R., Crouzet, N., Deming, D., & Madhusudhan, N. 2014, The Astrophysical Journal, 791, 55
- Nascimbeni, V., Piotto, G., Pagano, I., Scandariato, G., Sani, E., & Fumana, M. 2013, AAP, 559, A32
- Nichols, J. D., et al. 2015, APJ, 803, 9
- Nikolov, N., et al. 2015, MNRAS, 447, 463
- Pont, F., Sing, D. K., Gibson, N. P., Aigrain, S., Henry, G., & Husnoo, N. 2013, MNRAS, 432, 2917
- Poppenhaeager, K., Wolk, S. J., & Schmitt, J. H. M. M. 2015, in Cambridge Workshop on Cool Stars, Stellar Systems, and the Sun, Vol. 18, 18th Cambridge Workshop on Cool Stars, Stellar Systems, and the Sun, ed. G. T. van Belle & H. C. Harris, 733–738
- Redfield, S., Endl, M., Cochran, W. D., & Koesterke, L. 2008, APJL, 673, L87
- Salz, M., Czesla, S., Schneider, P. C., & Schmitt, J. H. M. M. 2016, AAP, 586, A75
- Sing, D. K., et al. 2013, MNRAS, 436, 2956
- . 2015, MNRAS, 446, 2428

Sotin, C., et al. 2015, European Planetary Science Congress 2015, 10, EPSC2015

Stevenson, K. B., Bean, J. L., Madhusudhan, N., & Harrington, J. 2014a, APJ, 791, 36

Stevenson, K. B., Bean, J. L., Seifahrt, A., Désert, J.-M., Madhusudhan, N., Bergmann, M., Kreidberg, L., & Homeier, D. 2014b, AJ, 147, 161

Torres, G., Winn, J., & Holman, M. J. 2008, APJ, 667, 1324

Wolszczan, A. 1992, Science, 264, 538